Marsh induced backwater: the influence of non-fluvial sedimentation on a delta's channel morphology and kinematics

Kelly Sanks[1], John Shaw[2], Samuel Zapp[3], José Silvestre[1], Ripul Dutt[1], and Kyle Straub[1]

[1]Tulane University, Department of Earth and Environmental Sciences, 6823 St. Charles Ave, Blessey Hall, New Orleans, LA, USA, 70118
[2]University of Arkansas, Department of Geoscience, 340 N. Campus Dr., 216 Gearhart Hall, Fayetteville, AR, USA, 72703
[3]Louisiana State University, Department of Oceanography and Coastal Sciences, 1002-Q Energy, Coast and Environment Building, Baton Rouge, LA, USA, 70803

Correspondence: Kelly Sanks (ksanks@tulane.edu)

Abstract. We investigate the interaction of fluvial and non-fluvial sedimentation on the channel morphology and kinematics of an experimental river delta. We compare two deltas: one that evolved with a proxy for non-fluvial sedimentation (treatment experiment) and one that evolved without the proxy (control). We show that the addition of the non-fluvial sediment proxy alters the delta's channel morphology and kinematics. Notably, the flow outside the channels is significantly reduced in the
5 treatment experiment and the channels are deeper (as a function of radial distance) and longer. We also find that the treatment channels have the same width from the entrance to the shoreline, while the control channels get narrower as they approach the shore. Interestingly, the channel beds in the treatment experiment often exist below sea level in the terrestrial portion of the delta top creating a ∼0.7 m reach of steady, nonuniform backwater flow. However, in the control experiment, the channel beds generally exist at or above relative sea level, creating channel movement resembling morphodynamic backwater
10 kinematics and topographic flow expansions. Differences between channel and far-field aggradation produce a longer channel in-filling timescale for the treatment as compared to the control, suggesting that the channel avulsions triggered by a peak in channel sedimentation occur less frequently in the treatment experiment. Despite this difference, the basin-wide timescale of lateral channel mobility remains similar. Ultimately, non-fluvial sedimentation on the delta top plays a key role in the channel morphology and kinematics of an experimental river delta, producing channels which are more analogous to channels in global
15 river deltas, and which cannot be produced solely by increasing cohesion in an experimental river delta.

1 Introduction

River deltas are dynamic systems that accumulate sediment through the interaction of many processes occurring in the distributary channels, floodplain, and basin. The formation and movement of channels (channel kinematics) distributes fluvial sediment across the delta plain, leading to both active depocenters and quiescent regions that change location through time (i.e., river
20 avulsions) (e.g., Coleman, 1988; Straub et al., 2009; Hoyal and Sheets, 2009; Chadwick et al., 2020). The active depocenters are dominated by fluvial sedimentation, which includes sediment deposition in mouth bars, channels, and the delta front, as well as finer-grained overbank deposition adjacent to the river occurring during floods (e.g., Coleman, 1988; Paola et al., 2011;

Khan et al., 2013). The passive areas aggrade through fine-grained mineral sediment delivered from the ocean through waves, tides, and storms (e.g., Smith et al., 2015; Sanks et al., 2020), primary production of organic material via wetland vegetation

25 (e.g., Nyman et al., 2006; Holmquist et al., 2018, 2021; Kelsall et al., 2023), and/or redistribution of sediment from marsh edge erosion (e.g., Hopkinson et al., 2018; Valentine et al., 2023): the combination of which we refer to as non-fluvial (marsh) sedimentation.

Understanding and managing sediment accretion in rivers, floodplains, and adjacent wetlands remains a key strategy to mitigate the impacts of relative sea level rise (RSLR) worldwide. For example, Louisiana has planned and implemented both

30 engineered sediment diversions (e.g., the recently approved mid-Barataria sediment diversion) and artificial marsh creation projects (e.g., CPRA, 2017; Nittrouer et al., 2012; White et al., 2019) to reconnect the river to its wetlands and restore the coastal land area (e.g., Elsey-Quirk et al., 2019; CPRA, 2017; Peyronnin et al., 2017; Xu et al., 2019). Another strategy is engineered river avulsions, in which avulsion location can be optimized if the location of maximum channel sedimentation is known (Moodie and Nittrouer, 2021). On the short-term, the success of these mitigation strategies depend on the interaction

35 of channel and wetland aggradation (e.g., Kirwan and Megonigal, 2013; Paola et al., 2011), which can be maximized under certain conditions (Esposito et al., 2017). However, the implications of wetland-channel coupling over timescales longer than avulsions (10 - 10^3 years, depending on river delta) remain unclear.

The deposition of fluvial sediment is controlled by proximity to and the movement of channels in a river delta and the life of a delta depends on the intrinsic ability for a river to avulse (Slingerland and Smith, 2004). Fluvial sedimentation typically

40 occurs via topographic flow expansions in physical delta experiments (e.g., Hoyal and Sheets, 2009; Chatanantavet and Lamb, 2014; Sittoni et al., 2014; Shaw et al., 2018). As the river enters the basin, the channels lose confinement, which triggers rapid deposition at the mouth bar (e.g., Edmonds and Slingerland, 2007; Sittoni et al., 2014; Törnqvist and Bridge, 2002). The rapid deposition leads to an upstream migration of the depocenter, which is referred to as the morphodynamic backwater effect (Hoyal and Sheets, 2009). Eventually, this process leads to a channel avulsion, which is thought to occur at some distance upstream

45 of the shoreline and is related to channel superelevation (e.g., Edmonds et al., 2009; Shaw et al., 2021; Mohrig et al., 2000; Hajek and Wolinsky, 2012; Ganti et al., 2016b; Jobe et al., 2020). The location of avulsions appears to occur preferentially at the backwater lengthscale (Jerolmack and Swenson, 2007), which is defined as the channel depth divided by the energy slope for low-Froude number systems (e.g., Shaw and McElroy, 2016). This lengthscale serves as an estimate of the distance between a channel mouth and the location where the channel bed of a river drops below sea level (Paola and Mohrig, 1996).

50 Morphodynamic models of channel deposition suggest that avulsion locations depend on variable discharge of a river to move the location of maximum aggradation upstream, through scour during floods (e.g., Nittrouer et al., 2011, 2012; Chatanantavet et al., 2012; Ganti et al., 2016b; Chadwick et al., 2019). It is argued that when fluctuating flows are not present, the location of maximum deposition is inevitably at the channel mouth, producing topographic flow expansions (or morphodynamic backwater effects) that typically dominate the channel kinematics of physical delta experiments.

55 Avulsion locations scale with backwater length, but there appear to be multiple possible causes for this scaling. The backwater length, or the length of the river that is influenced by off-shore processes, is thought to be controlled by complex hydrodynamics of rivers (e.g., Lamb et al., 2012; Chatanantavet et al., 2012; Nittrouer et al., 2011). More recently, Ratliff et al. (2021)

and Prasojo et al. (2022) show that avulsion locations on a river delta can be explained without backwater hydrodynamics and are a function of a break in slope in the channel (i.e., morphology of the channel). In other words, even though avulsion location scales with backwater length, Ratliff et al. (2021) suggest that avulsion locations and subsequent channel movement can be explained simply through change in geometry without the need for complex backwater hydrodynamics. Similar to Ratliff et al. (2021), Moodie et al. (2019) showed that a decrease in channel slope (i.e., a change in channel geometry) triggers lobe progradation, subsequently moving the location of maximum channel aggradation (and the avulsion location) further upstream. Relatedly, Sanks et al. (2022) showed that non-fluvial aggradation near the coastline can significantly rearrange depositional patters on experimental deltas, influencing delta hypsometry and floodplain geometry.

Despite these different mechanisms for avulsions, the impact of non-fluvial sedimentation on channel kinematics of deltaic systems remains largely unknown (Paola et al., 2011). While channel morphology and kinematics of river deltas in experimental (e.g., Hoyal and Sheets, 2009; Li et al., 2017; Straub et al., 2013; Barefoot et al., 2021; Carlson et al., 2018), numerical (e.g., Edmonds et al., 2009; Caldwell and Edmonds, 2014; Lauzon and Murray, 2018), and field settings (e.g., Shaw et al., 2016; Wilson and Goodbred, 2015; Aslan et al., 2005; Carlson et al., 2021) are well documented, wetland dynamics are rarely seen as coupled to, or a driver for, channel dynamics. In numerical and experimental settings, added sediment cohesion is often used to represent the influence of vegetation on the delta top for its ability to increase critical shear stresses and reduce erosion (e.g., Hoyal and Sheets, 2009; Edmonds and Slingerland, 2010; Li et al., 2017). Another numerical study shows that there is an optimal vegetation height for inorganic sediment trapping on deltaic marsh platforms (Nardin and Edmonds, 2014). Similarly, Piliouras et al. (2017) used alfalfa to simulate vegetation in an experimental delta, which showed enhanced sediment trapping and increased delta top roughness. Because the alfalfa increased the delta top slope, they found that results of the experiments were only applicable to fan deltas and not the low-sloping coastal deltas of interest here. While valuable, these previous studies leave out a critical property of wetlands, which is the ability to accumulate non-fluvially delivered sediment in-situ via primary production of vegetation (i.e., accumulation of above and belowground biomass) (e.g., Kosters et al., 1987; Morris et al., 2002; Mudd et al., 2009) and accumulation of fine-grained mineral sediment (muds) presumably delivered from the ocean (e.g., Leonardi et al., 2021; Sanks et al., 2020). In contrast to this body of work, Sanks et al. (2022) and Zapp (2020) show that non-fluvial sedimentation can act independent of cohesion, by changing the distribution of elevations, delta top slope, sediment partitioning, and shallow compaction rates.

To test the control of non-fluvial sedimentation on channel kinematics, we separate the broad variation in delta top facies, into "non-fluvial" (e.g., wetlands, interdistributary bays, tidal flats) and "fluvial" (e.g., upper delta plain, levees, mouth bars, prodelta) components (Bhattacharya, 2006). We define non-fluvial sedimentation as the spatially extensive, persistent, fine-grained, and compactable deposition that occurs in the quiescent, protected regions of deltas most commonly associated with wetland platforms (Fig. 1). In contrast, the fluvial sediment that is the default on experimental deltas is coarser grained, less compactable, and not persistent. If a small amount of non-fluvial sedimentation can significantly rearrange delta mass balance (Sanks et al., 2022), then it is possible for it to affect channel dynamics as well. We investigate this hypothesis here.
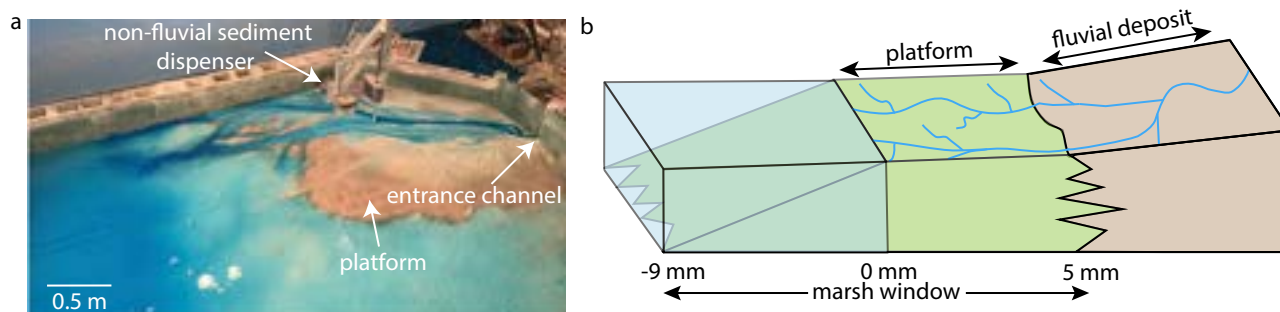
Figure 1. (a) Aerial image from the treatment experiment adapted from Sanks et al. (2022) showing the entrance channel, which delivers water and fluvial sediment to the delta top and the marsh sediment dispenser, which delivers non-fluvial sediment to the delta top. The brown sediment is the kaolinite marsh proxy, which forms a platform near sea level. (b) Conceptual diagram of a delta-wetland system adapted from NASA (2014). The platform, which aggrades through a combination of fluvially delivered fine-grained sediment, muds and organics delivered from off-shore, and organic sediment produced in-situ by vegetation, encompasses the area of the delta between 5 and -9 mm relative to sea level in the treatment experiment. The fluvial deposit exists above 5 mm relative to sea level and aggrades solely through the deposition of fluvially-delivered sediment.

2 Methods

2.1 Experimental Setup and Data

We compare two experiments run under the same boundary conditions (see Sanks et al. (2022) for in-depth methods), except one experiment has a proxy for non-fluvial (marsh) sedimentation (treatment) and one does not (control). The addition of the kaolinite marsh proxy accounts for ~15% of the final delta volume and ~8% of the mass in the treatment experiment. Thus, we assume that any changes in channel kinematics can be attributed directly to this non-fluvial sedimentation. Despite the differences in scale of field and experimental systems, physical experiments approximate conditions and processes that occur in global systems (Paola et al., 2009). Thus, physical delta experiments are an ideal way to study the influence of non-fluvial sedimentation on channel morphology and kinematics. Both experiments were run for 560 hours or ~20 times the compensation timescale to capture autogenics and account for the inherent stochasticity of the systems (Wang et al., 2011). Ultimately, the systems accumulate about 20 channel depths of stratigraphy, as the channels are ~7 mm deep and the deltas evolve with a background sea level rise rate ($RSLR_b$) of 140 mm over 560 hours.

We deposit non-fluvial sediment in the treatment experiment through an elevation-based model (marsh window, Fig. 1b). Elevation relative to sea level (rsl) is a primary control on the deposition of mud in tidal flats and wetland platforms, as well as organic sediment production in wetlands. Thus, an elevation-based model is representative of all non-fluvial sedimentation that occurs in deltaic coastal environments. Note that we neglect the hydrodynamics produced by vegetation in this study, as we are interested solely in the impact of additional mass that accumulates in global deltas on the long-term dynamics of the system. We adapt a model tying primary production in salt marshes to elevation relative to mean high tide from Morris

et al. (2002) and simplify this model to produce three distinct regions of non-fluvial deposition: unstable (-9 to -5 mm rsl),
110 maximum production (-5 to 0 mm rsl), and stable (0 to 5 mm rsl). The non-fluvial sediment is Edgar Plastic Kaolin (a type of
kaolinite) that we deposit from above using a sieve. Deposition rates are determined using a hexagonal grid (7.5 cm sides) to
find the average elevation inside each hexagon. If the average elevation falls within one of the three regions, we deposit either
3.4 g (maximum production; accumulates $1RSLR_b$) or 1.7 g (stable and unstable; accumulates $0.5RSLR_b$) of kaolinite every
two hours in that hexagon. The deposition rate was calibrated based on the assumption that kaolinite deposited in water has a
115 porosity of 90% (see Sanks et al. (2022) for more details).

To analyze the channel properties and kinematics from both experiments, we use dry and wet LiDAR scans, binary channel
maps, and binary flow maps (Appendix A). We collect dry LiDAR scans every hour for the control and every 2 hours for
the treatment while the experiments are paused. We collect wet LiDAR scans every hour for both experiments while they
are running. We create binary channel maps by hand mapping the channels using aerial imagery from both experiments (Fig.
120 A1). While it was recently shown that particle imagey velocimetry can capture channel motion, results are similar to hand
mapping techniques (Chadwick et al., 2022). Further, simple color thresholds are unable to differentiate between channelized
and non-channelized flow. Though hand mapping channels introduces human bias (Appendix A; Fig. A1), it has a negligible
impact on our results as compared to other methods (e.g., a color threshold). However, a simple color threshold can capture
total flow on the delta top (Fig. 3c,d), so we use this method to create total flow maps. As such, overbank flow maps can be
125 produced by differencing the total and channel flow maps. While overbank maps are sensitive to thresholding, the main results
are insensitive to threshold choice.

2.2   Channel Properties

We analyze the treatment and control experiments for differences in channel properties, such as trunk channel depth (H_{tc}),
channel planform area (A_c), channel length (L_c), and trunk channel width (W_{tc}). Channel properties are calculated for each
130 channel segment within a radial transect. Channel depths are calculated every 5 mm (width of one LiDAR pixel) from the apex
(0 mm) to 3100 mm (max channel length) from the apex, while all other channel properties are calculated every 50 mm from
the apex (0 mm) to 3100 mm from the apex because mean properties are not sensitive to bin width.

To calculate channel depths, we use a square channel buffer of 20 mm (4 pixels) on all sides of the channel maps to ensure
levee crests are captured in the measurement. H_c (mm) is then given by:

135 $$H_c = max(z_c) - min(z_c), \tag{1}$$

where $max(z_c)$ is the maximum channel elevation for each channel within in the radial transect (i.e., levee crest; Fig. 2c,d) and
$min(z_c)$ is the minimum channel elevation for each corresponding channel in the radial transect (i.e., channel thalweg; Fig.
2c,d). We produce a trunk channel depth (H_{tc}; mm) for each radial segment through time by:

$$H_{tc} = max(H_c). \tag{2}$$

140 We use these data to plot the median and interquartile range for H_{tc} as a function of distance from the apex. We also
determine the basin wide $\overline{H_c}$, which is simply the mean of all channel depths through space and time.

Basin wide channel area (A_{cb}; cm^2) is the time-averaged channel area (A_c). A_c is simply the sum of all channel pixels on the delta top multiplied by 0.25 cm^2 (the area of one pixel). Mean radial channel fraction $\overline{f_{Ac}}$ is then given by:

$$\overline{f_{Ac}} = \frac{A_{cr}}{A_r}, \tag{3}$$

145   where A_{cr} is the time-averaged channel area of the radial transect and A_r is the area of the radial transect.

L_c is assumed to be the straight line distance from the entrance channel to the most distal channel pixel at each timestep. We note that this is an underestimate for the length of any sinuous channels in the experiments.

W_{tc} is the trunk channel width (cm), and given by:

$$W_{tc} = max(A_{cr}/L_r), \tag{4}$$

150   where A_{cr} is the area of each channel in the 5 cm radial bin of interest (cm^2) and L_r is 5 cm, which is the length of the each radial bin. We note that this is likely an overestimate at the channel tips if the channelized portion in the last radial transect does not encompass the entire length of the radial bin.
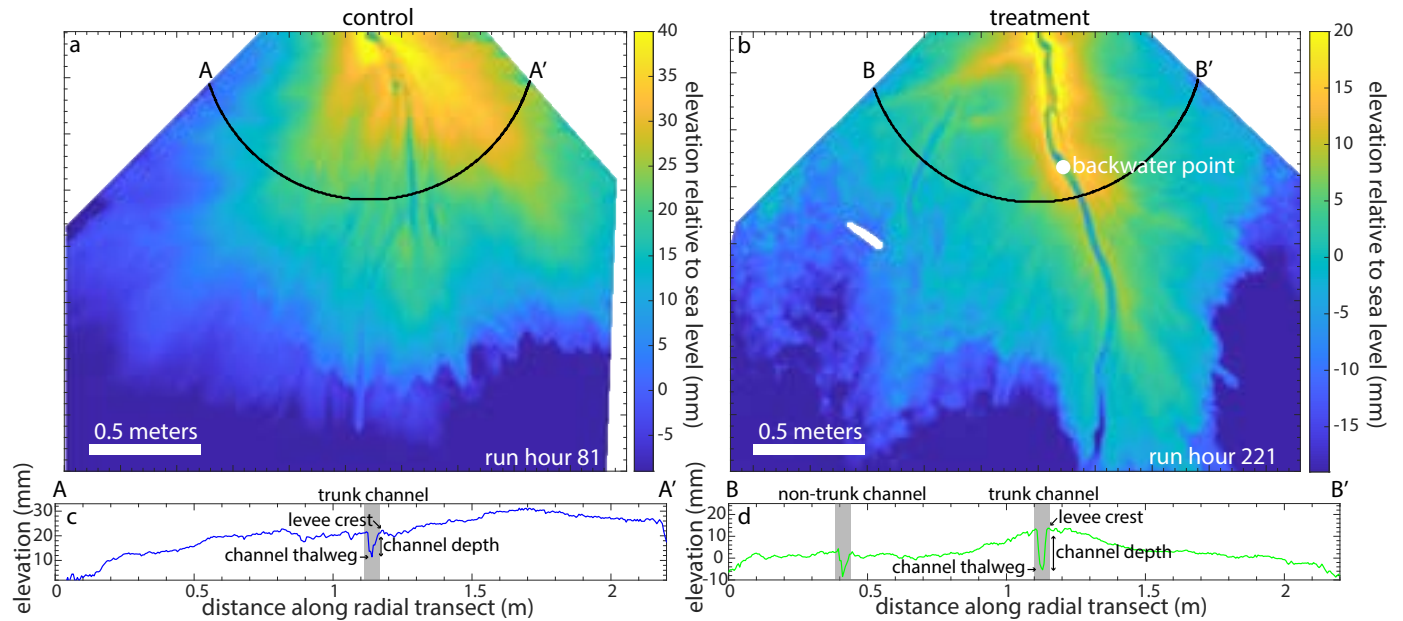
Figure 2. (a) LiDAR map of the control delta at run hour 81 showing elevations relative to sea level. The black line represents the transect A-A', which is 1 m from the apex. See Fig. 8a for aerial image. (b) LiDAR map of the treatment delta at run hour 221 showing elevations relative to sea level. The black line represents the transect B-B', which is 1 m from the apex. See Fig. 8b for aerial image. (c) Elevation relative to sea level versus the distance along the radial transect A-A'. (d) Elevation relative to sea level versus the distance along the radial transect B-B'.

We are also interested in the hydrodynamic backwater effects present in both experiments. We define the hydrodynamic backwater length as the longest continuous length of the channel reach that exists at or below sea level (Chatanantavet et al.,

155   2012). To calculate the length of the backwater reach, we use dry LiDAR scans and channel maps at one (control) and two
(treatment) hour intervals (n = 560 for the control and n = 265 for the treatment due to artifacts rendering 15 timesteps
unusable). We determine the location of beginning of the longest continuous backwater reach and this location is referred to
as the backwater point (Fig. 2b). If the channel tip is above sea level or there is no radial channel transect with at least 16% of
channel bed elevations at or below sea level, then there is effectively no backwater reach and we assume the backwater length
160   is zero.

2.3   Channel Kinematics

Various metrics were used to compare channel kinematics between the experiments. The delta top area used to quantify lateral
channel movement is defined as the area above sea level for at least 50% of the experiment (p_{land}; Fig. B1), consistent with Li
et al. (2017). We compute the fraction of the delta (delta area $= p_{land}$; m^2) that has not been visited by a channel through time,
165   which can be used to estimate the lateral channel mobility of the system (Li et al., 2017). This metric (f_{mob}; -) is defined as:

$$f_{mob} = \frac{\sum\limits_{i}^{n} A_c}{p_{land}}, \tag{5}$$

where i is the initial hour and n is every time step from 1 to 560 (e.g., if using a time step $n > i$, the numerator is the cumulative
channel area from hours i through n (A_c; m^2). The unvisited area of the experiments decays exponentially through time. To
describe this, we compute the e-folding lateral mobility timescale (T_{mob}; hours). T_{mob} is the inverse of the exponent from
170   the function that describes the lateral channel mobility decay of the system (Li et al., 2017). Radial lateral mobility is also
calculated every 50 mm from the apex (0 mm) to 3100 mm from the apex. In this case, A_c is the channelized area in the radial
transect and p_{land} is the area of the radial transect. Similarly, we calculate the planform overlap decorrelation metric described
in Wickert et al. (2013) as an independent check on the lateral mobility of the system. This metric describes the time it takes
for subsequent channel maps to decorrelate. Both the lateral channel mobility and planform overlap indirectly describe the
175   avulsion timescale. Planform overlap is described in Appendix B (see also Fig. B5).

We then calculate channel mobility metrics related to sedimentation patterns on the delta, as channel sedimentation can
trigger an avulsion (e.g., Jobe et al., 2020; Ganti et al., 2016b; Moodie and Nittrouer, 2021). The first is the fraction of the delta
that is unmodified (f_{um}; -), which is defined as the fraction of the delta that has accumulated at least 1 mm of sediment in the
terrestrial delta (p_{land}) for various periods of time. Similar methods to the lateral mobility are used to determine f_{um} (Li et al.,
180   2017). The modification timescale (hours) is the inverse of the exponent from the function that describes how long it takes to
accumulate 1mm of sediment in the terrestrial delta.

Secondly, we calculate the compensation timescale (T_c; hours). Compensation is a metric used to describe surface processes
in channelized systems and compares long-term sedimentation patterns to general accommodation of the system. In general,
compensation describes a channel's inherent tendency to fill low-lying areas on the delta (Straub et al., 2009). T_c refers to how
185   long it takes to accumulate roughly one channel depth of sediment everywhere on the delta top. Again, to capture levee crests
in the channel depths, we use a square channel buffer of 20 mm (4 pixels) on all sides of the channel maps. Basin-wide T_c is

given by:

$$T_c = \frac{H_c}{V_t},\tag{6}$$

where H_c is the basin-wide mean channel depth (mm) and V_t is 0.25 mm/hr, which is the mean aggradation rate for both

190 experiments. T_c is also calculated radially from the apex using 5 mm bins, where H_c is the mean trunk channel depth (mm) of the radial bin and V_t is the mean total aggradation rate (mm/hr) of the radial bin. To directly compare aggradation rates between the experiments at the same timescale (Sadler, 1981), we use 2-hour LiDAR difference maps for both experiments.

Lastly, we determine the channel in-filling timescale (T_f; hours). Avulsion locations can be related to peaks in channel aggradation (e.g., Chatanantavet et al., 2012; Chadwick et al., 2019; Moodie and Nittrouer, 2021), so we calculate channel and

195 far-field aggradation rates (mm/hr), allowing us to compare channelized (channel) and non-channelized (far-field) sediment depositional patterns. We again use the buffered channel maps and compute aggradation rates every 2-hours. The channel in-filling timescale (T_f; hrs) is given by:

$$T_f = \frac{H_c}{V_c - V_{ff}},\tag{7}$$

where H_c is the basin-wide mean channel depth (mm), V_c is the basin wide channel aggradation rate (mm/hr), and V_{ff} is the

200 basin wide far-field aggradation rate (mm/hr). We also compute a channel in-filling timescale radially from the apex every 5 mm. In this case, H_c is the time-averaged trunk channel depth for each radial transect, V_c is the time-averaged channel aggradation rate (mm/hr) for each radial transect, and V_{ff} is the time-averaged far-field aggradation rate (mm/hr) for each radial transect.

3 Results

205 ### 3.1 Channel Properties

Does the presence of non-fluvial sedimentation influence channel morphology in experimental deltas? A simple comparison reveals significant differences. Importantly, there is a difference in the fraction of the delta top covered in overbank flow (0.489 $\pm$ 0.119 in the control and 0.183 $\pm$ 0.122 in the treatment, Fig. 3) or a reduction in overbank flow by about one fourth in the treatment as compared to the control. Though this decrease in overbank flow does not lead to an increase in planform channel

210 area, it does suggest that the flow is concentrated in channels in the treatment experiment. A loss of channel confinement is observed, associated with an increase in overbank flow, in both the control and treatment experiments near the mean shoreline (Fig. 3a and b).

The basin-wide channel morphology of the control and treatment experiments are different (Table 1). The channels are on average narrower (Fig. 4b) and longer (Fig. 4c) in the treatment experiment as compared to the control. Further, the treatment

215 experiment has a greater number of distributary channels on the delta top (Fig. 4d).

The channels in the treatment and control experiments extend past the mean shoreline (Figs. 4a and 4c). The mean shoreline in the control experiment is 0.942 $\pm$ 0.156 m (blue diamonds in all radial Figs.) and the mean channel length is 1.51 $\pm$ 0.211
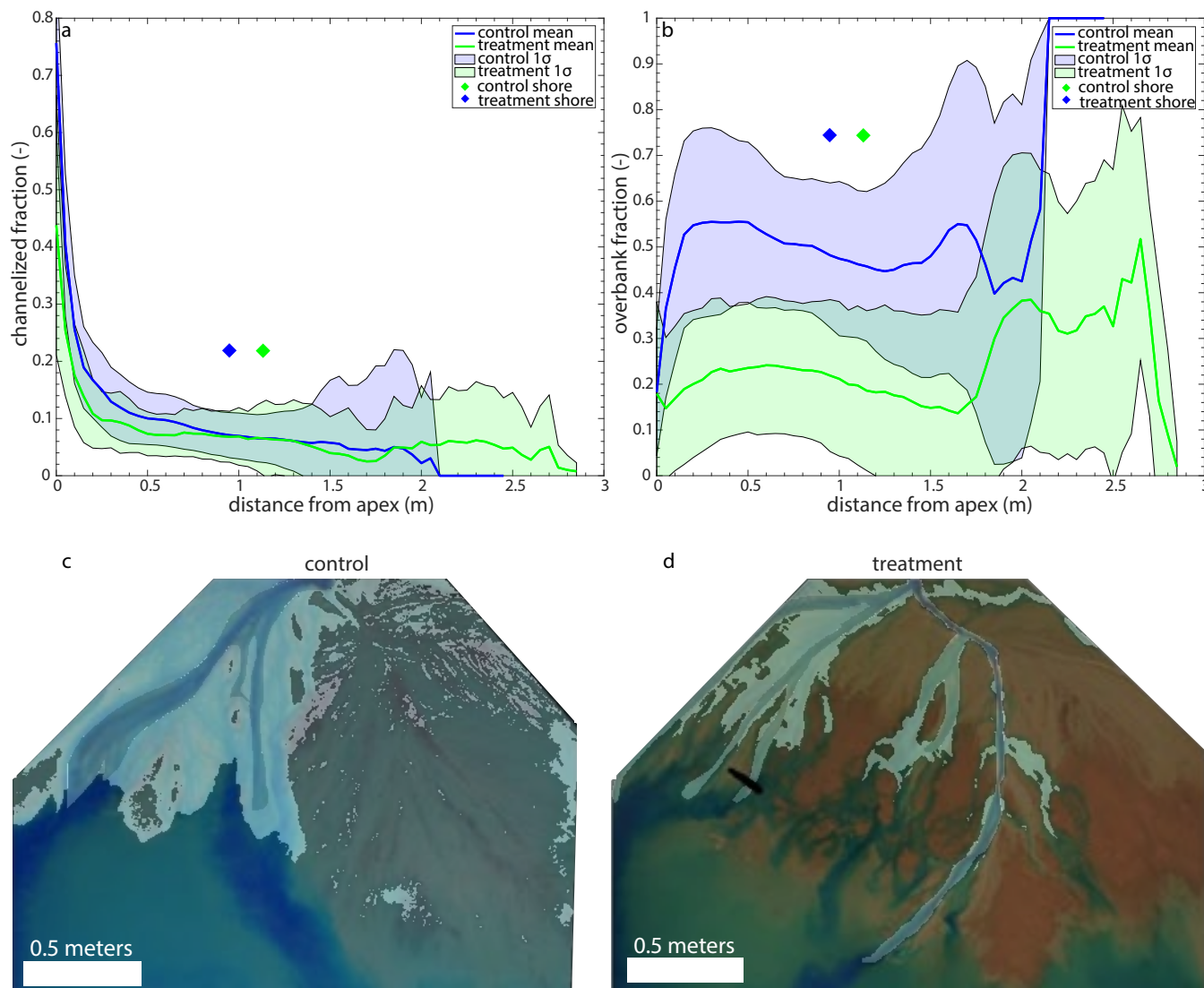
Figure 3. (a) Mean channelized and (b) overbank flow fraction as a function of distance from the apex for the control (blue) and treatment (green) with 1σ standard deviation shown in the shaded polygons. (c) The channelized and overbank flow on the terrestrial delta top for the control experiment at hour 181, which approximates mean flow conditions during the experiment. (d) The channelized and overbank flow on the terrestrial delta top for the treatment experiment at hour 360, which approximates mean flow conditions during the experiment.

m. On average, the channels extend 0.571 ± 0.265 m past the mean shoreline. The mean shoreline in the treatment experiment is 1.11 ± 0.156 (green diamonds in all radial Figs.) and the mean channel length is 1.90 ± 0.420. On average, the channels extend 0.793 ± 0.413 m past the mean shoreline. While the slope break occurs around the median shoreline for the treatment experiment (i.e., the overstepped channels have a slope break), there is no such break in the control (Fig. 4a), even though the

Table 1. Basin-wide channel properties for the control and treatment experiments.

Channel Property	Control	Treatment	Treatment:Control Ratio
mean channel area (m^2)	0.189 ± 0.0510	0.215 ± 0.0628	1.14
mean overbank flow area (m^2)	1.07 ± 0.310	0.451 ± 0.308	0.422
channel:overbank ratio (-)	0.191 ± 0.0749	1.29 ± 3.96	6.75
mean trunk channel width (cm)	8.96 ± 5.21	5.97 ± 3.42	0.666
mean channel length (m)	1.51 ± 0.211	1.90 ± 0.420	1.26
mean channel depth (mm)	6.64 ± 6.29	6.65 ± 6.09	1.00
mean backwater length (m)	0.0474 ± 0.0883	0.683 ± 0.341	14.4
mean channel aggradation (mm/hr)	0.425 ± 1.23	0.450 ± 1.15	1.06
mean far-field aggradation (mm/hr)	0.050 ± 2.21	0.100 ± 1.38	2.00
compensation timescale (hrs)	26.6	26.6	1.00
lateral mobility timescale (hrs)	62.9	60.4	0.960
modification timescale (hrs)	28.7	17.4	0.606
channel in-filling timescale (hrs)	8.70	13.8	1.59

channels extend past the mean shoreline as well. The channel beds in the treatment are often below mean sea level, suggesting the presence of hydrodynamic backwater effects (Fig. 4a). However, this is not the case in the control, as the channels are perched slightly above sea level, suggesting the channels do not always extend past the local shoreline. The channels in the

225 treatment experiment have a slope break that occurs on average around 1.5 m from the apex, whereas the channels in the control experiment have the same slope for the entire length. The channels in the control experiment are wider near the apex and get narrower as they approach the shoreline, whereas the treatment channels have a more constant width as a function of distance from the apex (Fig. 4b). Though the width is less variable, the treatment channels do narrow past the mean shoreline. Further, the treatment has more channels on the delta top at any one time than the control experiment (Fig. 4d). The combination of

230 more and longer channels in the treatment experiment produces channels with similar planform area (Table 1). The number of channels decreases with radial distance from the apex in both experiments, supporting loss of channel confinement near the shoreline.

How does the addition of marsh deposition affect the presence of a backwater reach? We show that the treatment experiment has a significant backwater reach that is not observed in the control experiment (Fig. 5). Out of the 560 hours of the control

235 experiment, there is no radial transect with at least 16% of elevations at or below sea level for 49% of the experiment (274 hours). Of the 286 hours in the control experiment with an observed backwater reach, 99% of the channels have backwater lengths <= 0.5 m, with a maximum backwater length of 0.57 m (Fig. 5). However, a backwater length is always observed in the treatment experiment for the 265 hours where there is a viable channel map. The treatment experiment has a backwater
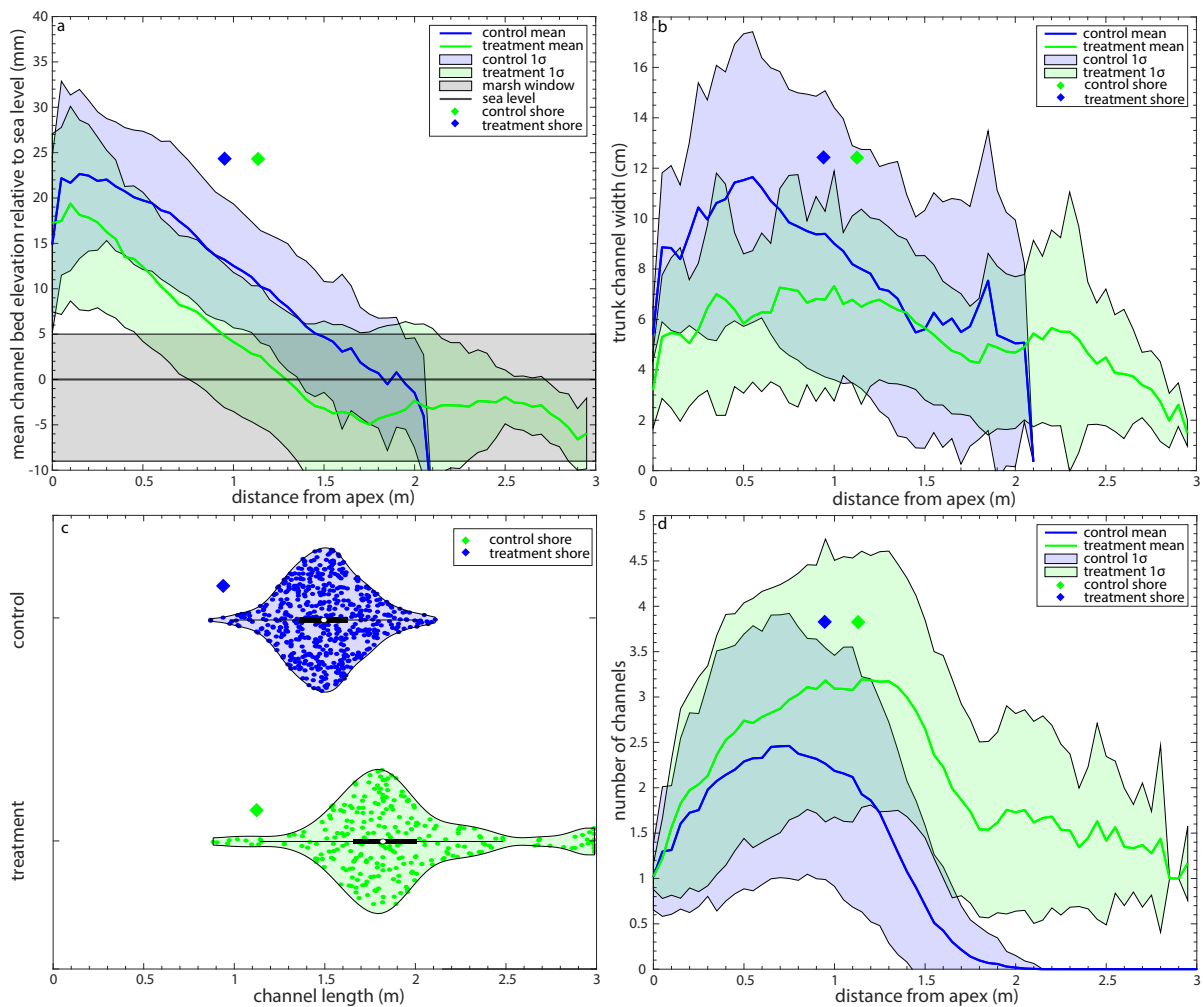
Figure 4. Channel morphology for the control (blue) and treatment (green) experiments. (a) The mean channel bed elevation relative to sea level (mm) as a function of radial distance from the apex (m). (b) The mean trunk channel width (cm) as a function of radial distance from the apex (m). (c) Violin plots of the channel length (m) for the control and treatment experiments. (d) The mean number of channels as a function of distance from the apex (m). Shaded blue (control) and green (treatment) area signifies 1σ standard deviation from the mean.

length > 0.5 m 69% of the time, with a maximum backwater length of 1.91 m (Fig. 5). The average backwater length in the
240 control experiment is 0.0474 m and 0.683 m in the treatment (Table 1, Fig. 5).
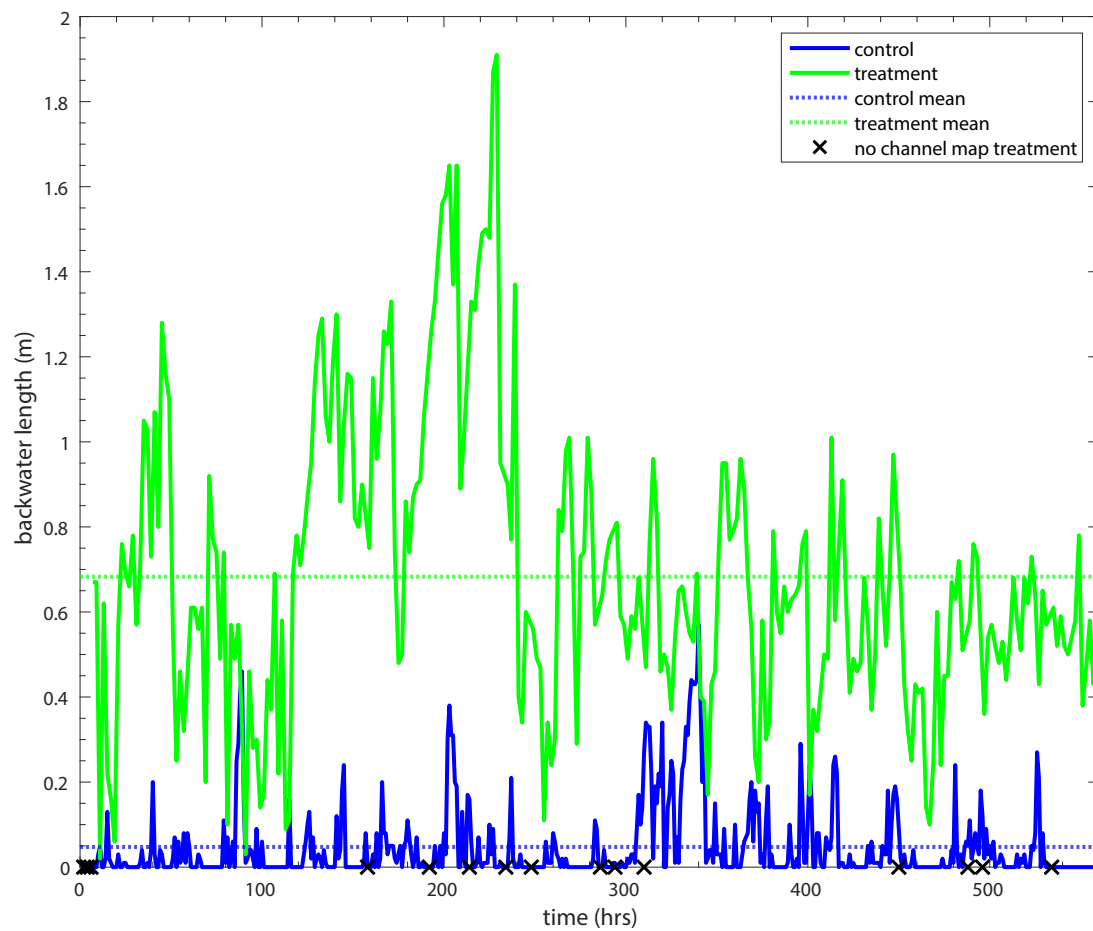
Figure 5. The backwater length (m), measured as the maximum consecutive length of the channel domain that is at or beneath sea level, for the control (blue) and treatment (green) experiments through time. The black x's represent the times with no channel maps for the treatment experiment.

3.2 Channel Kinematics

Despite the differences in channel morphology, we observe only subtle differences in statistics characterizing channel kinematics, or the motion of the channels. We first characterize channel and far-field aggradation rates for both experiments and observe differences (Fig. 6). The mean channel aggradation rate in the control experiment increases with radial distance from
245 the apex with a large peak near the downstream end, characteristic of topographic flow expansions (Fig. 6a). In contrast, the treatment experiment shows a significantly reduced peak in mean channel aggradation rates near the shoreline (Fig. 6a).
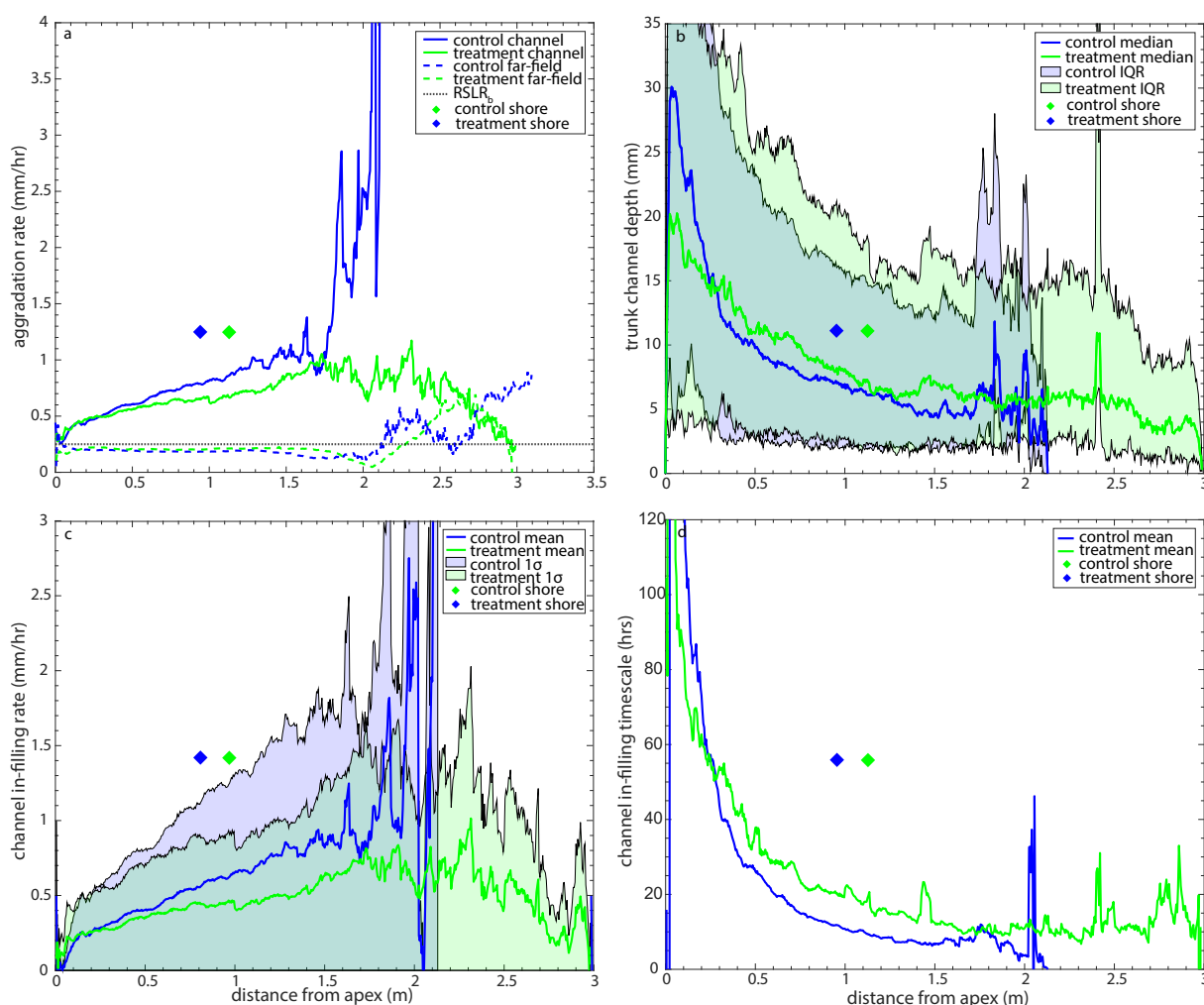
Figure 6. (a) The mean channel (solid line) and far-field (dashed line) aggradation rates (mm/hr) in the control (blue) and treatment (green) experiments as a function of radial distance from the apex (m). (b) The median trunk channel depth (mm) as a function of radial distance from the apex (m). (c) The aggradation difference (mm/hr) (i.e., the channel in-filling rate) between far-field and channel aggradation rates as a function of radial distance downstream (m). (d) The channel-infilling timescale (hrs) as a function of radial distance downstream (m).

Sediment accumulation rates show that the mean basin-wide channel aggradation rate for the control experiment is 0.425 $\pm$ 1.23 mm/hr and 0.450 $\pm$ 1.15 mm/hr for the treatment. The basin-wide mean far-field aggradation rate for the control is 0.050 $\pm$ 2.21 mm/hr and 0.100 $\pm$ 1.38 mm/hr for the treatment. Because, the basin-wide channel depths are the same for both
250   experiments, this results in a basin-wide channel in-filling timescale (T_f) of 8.70 hours for the control and 13.8 hours for the treatment experiment (using Equation 7). It takes about 1.5 times as long for channels to fill in relative to the floodplain in the treatment experiment than the control, suggesting the presence of channel buttressing via the non-fluvial sedimentation in the treatment experiment. Despite similar basin-wide channel depths, the trunk channels in the treatment experiment are deeper than in the control (Fig. 6b), again producing a longer T_f as a function of radial distance from the apex (Fig. 6d).

255   Both control and treatment experiments exhibited mobile channels with some clear episodes of avulsion and lateral migration (Appendix B). However, the steady presence of shallow unchannelized flow in both experiments made it impossible to map discrete avulsion locations. Instead, both deltas appeared to maintain overbank flows that kept the "finding phase" (Reitz et al., 2015) of the avulsion cycle active (Figs. B3, B4). No clear distinction in avulsion location or timescale could be established despite the significant difference in backwater length and aggradation patterns.

260   The basin-wide lateral mobility is roughly the same in both experiments (Fig. 7a). The basin-wide lateral mobility timescale (T_{mob}) for the control experiment is 63 hours and 60 hours for the treatment experiment (Fig. 7a). However, we see subtle differences in T_{mob} as a function of radial distance from the apex (Fig. 7c,d). The channels on the terrestrial delta top (i.e., p_{land}) move slightly slower in the treatment as compared to the control. Lateral channel movement increases slightly as the channels approach the mean shoreline in the treatment, whereas channel movement is similar across the terrestrial delta top in
265   the control. Similar to the T_{mob}, the planform overlap metric (another proxy for an avulsion timescale; Wickert et al. (2013)) shows little difference between control and treatment experiments (Appendix B, Fig. B5). However, it takes about one-half the time to modify 90% delta top by at least 1 mm in the treatment as compared to the control experiment (Fig. 7b), which agrees with the channel and far-field channel aggradation rates and is due to the addition of the non-fluvial proxy in the low-lying region of the delta top. Thus, the addition of non-fluvial sediment in the marsh window ($\sim$0.25 mm/hr for areas in the
270   stable marsh window) is more widespread and outpaces (on a short-term scale) the far-field sediment deposition of the control experiment. Relatedly, because the channels are the same depth (basin-wide mean; Equation 1) and the experiments both have long-term, basin-wide aggradation rates of 0.25 mm/hr (or RSLR$_b$), basin-wide (T_c; Equation 6) is the same.
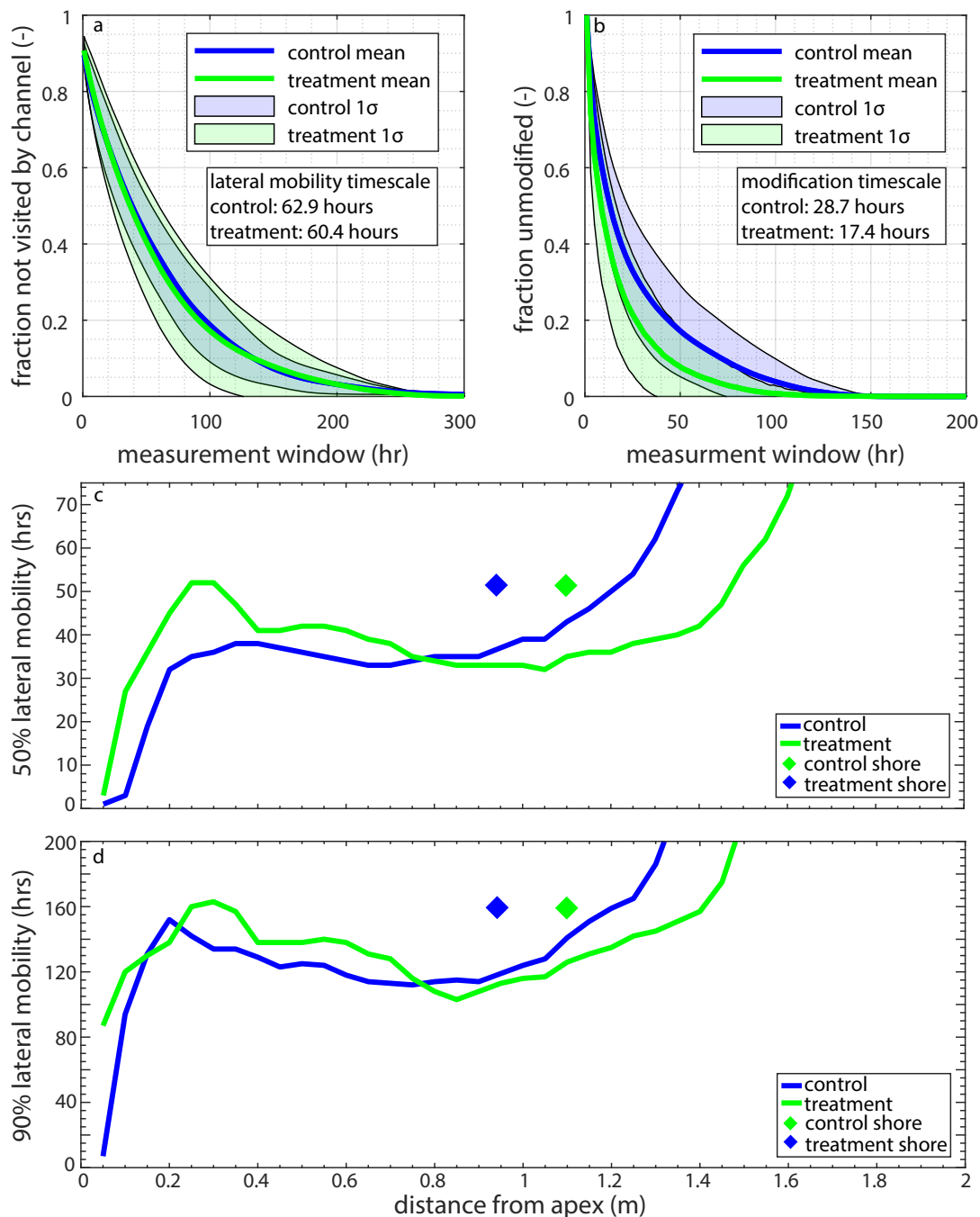
Figure 7. (a) The fraction of the delta not visited by a channel for the control (blue) and treatment (green) experiments versus time in run hours. (b) The fraction of the delta top that has not accumulated at least 1 mm of sediment for the control (blue) and treatment (green) experiments versus time in run hours. (c) The 50% lateral channel mobility (hrs), or how long it takes the channels to visit 50% of the radial transect, as a function of radial distance from the apex (m) for both experiments. (d) The 90% lateral channel mobility (hrs), or how long it takes the channels to visit 90% of the radial transect, as a function of radial distance from the apex (m) for both experiments.

4 Discussion

4.1 The impact of non-fluvial deposition on deltaic channel evolution

275 The impact of the non-fluvial deposition is to make longer channels that must traverse a slope break and a large platform near sea level (Fig. 8). The channels in the control experiment are wider on average, but typically turn into sheet flow before they reach the ocean basin (Fig. 8a; Appendix B; Figs. B3). These channels are characterized by topographic flow expansions (Sittoni et al., 2014) and distally increasing deposition rates, indicating a morphodynamic backwater control on channel filling and migration. Because of high deposition rates in the lobes, the channels lose confinement before they reach the local shoreline

280 leading to abrupt backstepping just before channel avulsion occurs. The flow expansions occur in the distal channel lobes, but impact the channelization of the entire system, leading to 60% of the terrestrial delta being covered with flow on average. This mechanism of channel movement and fluvial sedimentation produces channels that only reach the local shoreline about 24% of the time, meaning that the backwater length is effectively zero. Thus, topographic flow expansions are the primary control on channel kinematics in the control experiment, which is similar to previous physical experiments without variable discharge

285 (e.g., Li et al., 2017; Hoyal and Sheets, 2009).
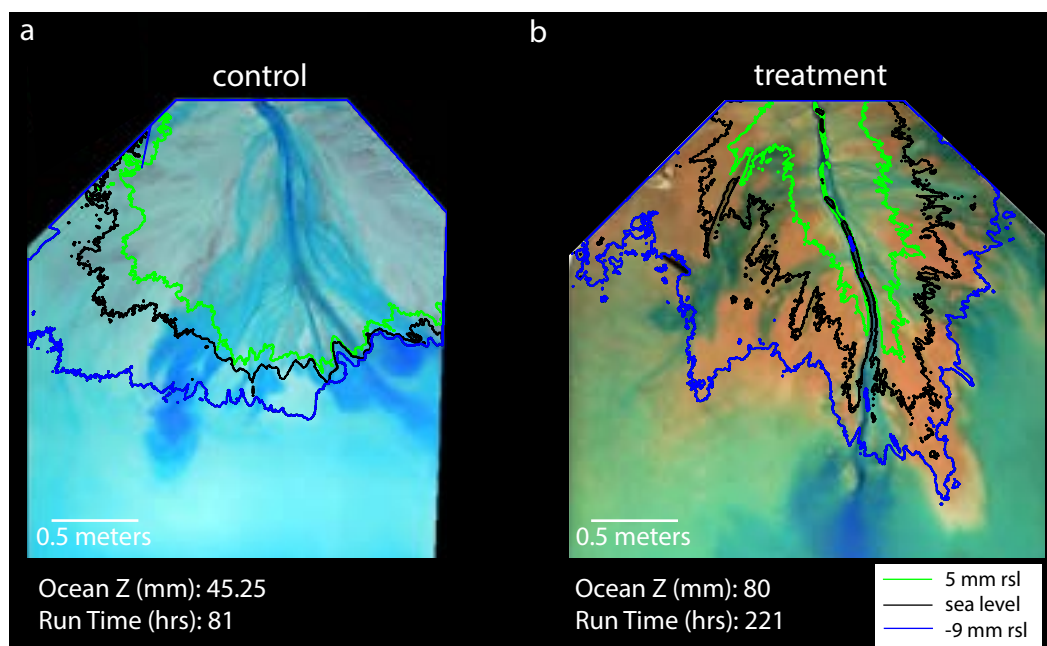
Figure 8. Control and treatment channel comparison. (a) Aerial image of the control delta top at run hour 81 with contour lines at 5 mm (green) relative to sea level (rsl), sea level (black), and -9 mm rsl (blue). (b) Aerial image of the treatment experiment at run hour 221 with contour lines at 5 mm rsl (green), sea level (black), and -9 mm rsl (blue).

Are topographic flow expansions also the dominant mechanism for channel movement in the treatment experiment? A dynamic network of feedbacks created from the deposition of non-fluvial sediment allows the system to exist in dynamic equilibrium with constant relative sea level rise, but with a very different morphology than the control experiment. Though we do observe topographic flow expansions and an increase in channel aggradation as the channels approach the basin indicating
290   the presence of morphodynamic backwater (Appendix B; Fig. B4), the dominant control is the presence of hydrodynamic backwater during 95% of the treatment experiment despite constant water discharge. We observe more distributary channels in the treatment experiment, but they are narrower (Fig. 4b), and the trunk channels are deeper (Fig. 6b) and longer (Fig. 4c) than in the control. This agrees with previous studies that show vegetation increases channelization and creates narrower, longer, and deeper channels (Lauzon and Murray, 2018). While these studies primarily focus on hydrodynamics, we show that the
295   extra mass accumulating in these vast wetland platforms impacts channel morphology in similar ways. The formation of more distributary channels offsets the narrower channels in the treatment experiment to keep channelized area similar between the two experiments. Further, flow is more constrained to the channels (Fig. 3b), indicating channel aggradation as the primary form of fluvial sedimentation.

It is evident from other studies that avulsion locations scale with the backwater length of rivers (e.g., Chatanantavet et al.,
300   2012). Sedimentation is supposedly maximized at this distance upstream of the shoreline, promoting an avulsion due to a higher channel super-elevation at this location. Interestingly, the addition of sediment in the low-lying overbank regions of the delta top creates channels that have a long backwater reach, without incorporating variable discharge and flood stages, as is often suggested (e.g., Lamb et al., 2012; Ganti et al., 2016a). While these constant discharge experiments both show increases in channel aggradation rate and decreases in avulsion timescale with distance downstream, the treatment experiment lacks
305   the significant increase in aggradation rate near the local shoreline that produced classic topographic flow expansions in the control experiment. These results suggest that the channel avulsions triggered by a peak in channel sedimentation occur less frequently in the treatment experiment as compared to the control. Recent research shows that avulsion locations may occur because of geometric constraints (e.g., a break in slope) and can be determined without backwater hydrodynamics (Ratliff et al., 2021; Prasojo et al., 2022). Unlike the control, the treatment experiment exhibits a channel slope break near the local
310   shoreline (Fig. 4a), and the channels usually extend past the local shoreline creating significant backwater lengths often >0.5m (Fig. 8). Because we did not alter the flow conditions (or hydrodynamics) between the two experiments and flow was held constant throughout the entire experiment, we suggest a new control on hydrodynamic backwater: non-fluvial sedimentation (i.e., wetland accretion). Thus, hydrodynamic backwater promoted by non-fluvial deposition has a strong control on channel kinematics in the treatment experiment, which is similar to global deltas (e.g., Ratliff et al., 2021; Chatanantavet et al., 2012;
315   Lamb et al., 2012). This has important implications for controls on avulsions and channel movement in field-scale deltas.

Surprisingly, the basin-wide timescale of lateral channel movement (T_{mob}) is similar in both experiments (Fig. 7a; Table 1). Previous research has shown that vegetation decreases the lateral mobility of channels, effectively slowing channel migration in experimental and field systems (Wickert et al., 2013; Tal and Paola, 2010; Ielpi and Lapôtre, 2020) due to increased channelization and enhanced bank stability. For this reason, we hypothesized that the treatment experiment would have a longer
320   T_{mob}, but this is not the case. The volume of fluvial sediment that accumulates on the terrestrial delta top is similar in the

two experiments (Sanks et al., 2022). Combined with the systems evolving under the same base level rise rates, the long-term distribution of fluvial sediment needs to be similar. Although we observe a smaller ratio of far-field aggradation to channel aggradation in the treatment experiment than the control experiment (by ∼50%) and the maximum channel aggradation is significantly reduced, compaction and other sediment properties create two systems with a similar terrestrial mass balance over

325 their lifespans (Sanks et al., 2022). Thus, it is actually unsurprising that basin-wide T_{mob} is similar. Despite these results, we observe subtle changes in lateral mobility as a function of distance from the apex (Fig. 7c and d), which shows that non-fluvial deposition in the treatment experiment decreases channel movement slightly for area of the delta that is less than 0.8 m from the apex as compared to the control, leading to longer timescales necessary to reach 50 and 90% of this area. However, this is associated with an increase in channel movement beyond this distance in both experiments that is likely related to an increase

330 in channel aggradation here.

4.2 Implications

Planned river diversions are a critical management strategy for river deltas threatened by sea level rise. New river channels will be formed and their morphology and kinematics will determine sediment deposition and accumulation; thus, understanding the interaction of fluvial and non-fluvial sedimentation is important for successful river diversions. While the distribution of

335 fluvial sediment is extremely important on short-timescales in these scenarios, the movement of the channels will control the long-term success of these engineering strategies. Our study suggests that channel and floodplain aggradation rates depend on the non-fluvial sedimentation occurring in the system. For example, wetland aggradation appears to decrease the rate of maximum channel aggradation and amount of overbank flow, so it is important to incorporate this into management plans.

We also show that non-fluvial sedimentation in the low-lying region of the delta top changes the morphology of the channels

340 and is the primary control of backwater effects in the experimental setting. Wetlands are deteriorating in many coastal deltas worldwide (e.g., Couvillion et al., 2017; Morton et al., 2015; Kirwan et al., 2010; Reed, 1995). If marshes are no longer present in the deltaic system, it is possible that the morphology of the entire delta and its channels will change. Thus, we suggest that channel sediment deposition in a field-scale delta without marshes may be influenced more by topographic flow expansions and morphodynamic backwater effects, as opposed to the hydrodynamic backwater effects that dominate most global deltas.

345 Further, river avulsions are potentially catastrophic for communities (e.g., Slingerland and Smith, 2004), which may lead to the eventual regulation of hydrodynamics (e.g., flood stages) to control the avulsion location and river slope break location in deltaic systems, similar to engineered avulsions based on river sedimentation proposed by Moodie and Nittrouer (2021). We show that the marsh platform and its floodplain deposition is enough to produce the slope break and subsequent "hy-drodynamic" backwater effect without changing hydrodynamics; thus, controlling the hydrodynamics of rivers may not be

350 necessary.

5 Conclusions

The addition of the marsh proxy in the experimental setting produced some surprising dynamics. The channel morphology of the two systems varies greatly. We show that in-situ accumulation of sediment in wetland platforms and tidal flats increases the trunk channel depth and number of distributary channels in deltaic systems, which allows the channels to extend further
355 into the basin. However, this non-fluvial deposition decreases the tendency for unchannelized (overbank) flow in the floodplain, effectively concentrating flow to the channels. In turn, the channels deposit sediment more consistently throughout the channel, significantly decreasing the channel aggradation peak near the shoreline that occurs in a control experiment and is characteristic of morphodynamic backwater. Importantly, the presence of non-fluvial sedimentation in the treatment experiment creates a long backwater reach without inducing variable discharge. Even though we observe these very clear differences in channel
360 morphology, the basin-wide timescale of lateral channel movement remains similar. The non-fluvial (marsh) sedimentation proxy produces a channel morphology of the treatment experiment more akin to that observed in global deltas, and thus the treatment experiment can be used to better understand the kinematics and long-term suitability of planned river diversions, avulsions, and general management strategies.

Code and data availability. Data used to reproduced the results of this study is available on FigShare (10.6084/m9.figshare.22320811).
365 Software used to reproduce the results of this study will be hosted in Zenodo upon review. The code is currently available on GitHub (https://github.com/kmsanks/TDWB_19_2_Channels) for review purposes. Data archiving of the raw experimental data is available at the "Tulane_Sediment_Dynamics_Stratigraphy_TSDS" project space: https://sead2.ncsa.illinois.edu/spaces/5825f529e4b0f3dd19c8d93a (TDB-18-1 [control] and TDWB-19-2-Surface-Processes [treatment]). Note, these data are not needed to reproduce any results from the study, but may be of interest for other researchers.

370 Appendix A: Channel Maps

Channel morphology and kinematics provide key insight into the life cycle and fate of a river delta (e.g., Edmonds et al., 2009). To determine channel morphology and kinematics in an experimental river delta, binary channel maps are needed. We use a software called ImageJ to hand map the channels in the experiments, as it retains basin coordinates. First, we load the RGB (red, green, blue) image (collected every hour from the wet LiDAR scans) into the software (Fig. A1a) and then use
375 the freehand selection tool to trace the outline of the channel map (Fig. A1b). Once the entire channel has been mapped, we export the channel map as a binary TIFF file (Edit -> Selection -> Create Mask). We use the resulting channel maps (Fig. A1c) to analyze various properties and kinematics of both the control and treatment experiments. The control experiment channels were mapped by Ripul Dutt and the treatment experiment channels were mapped by Kelly Sanks.
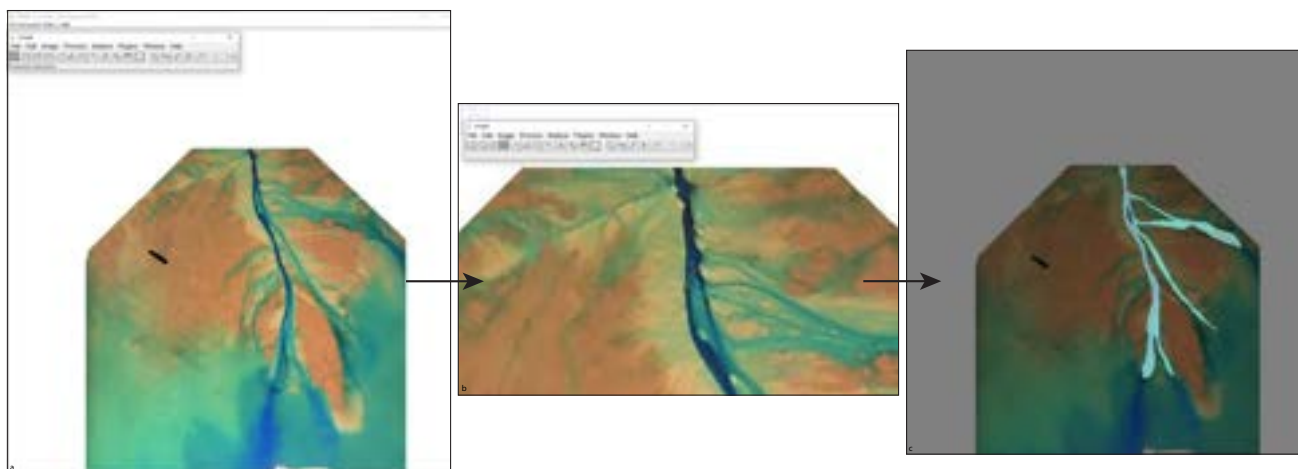
Figure A1. (a) An RGB image from hour 218 of the treatment experiment loaded into ImageJ. Note in the top right corner the image size is 750x747, which are the pixel dimensions of the LiDAR scans from the treatment experiment. (b) The yellow outline around the beginning of the channel illustrates one portion of channel map created using the freehand selection tool. The polygons were created by zooming into the channel creating a polygon around the channel. (c) The resulting channel map overlain on the RGB image for hour 218 of the treatment experiment.

Appendix B: Channel Kinematics

380   We use p_{land} as the delta area for most channel metric calculations, which describes the delta area that is above sea level for at least 50% of the experiment. This area is smaller in the treatment experiment ($\sim$2.0 m^2) than the control ($\sim$2.2 m^2), but the size and locations where the delta is above sea level in the treatment experiment are more variable (Fig. B1).
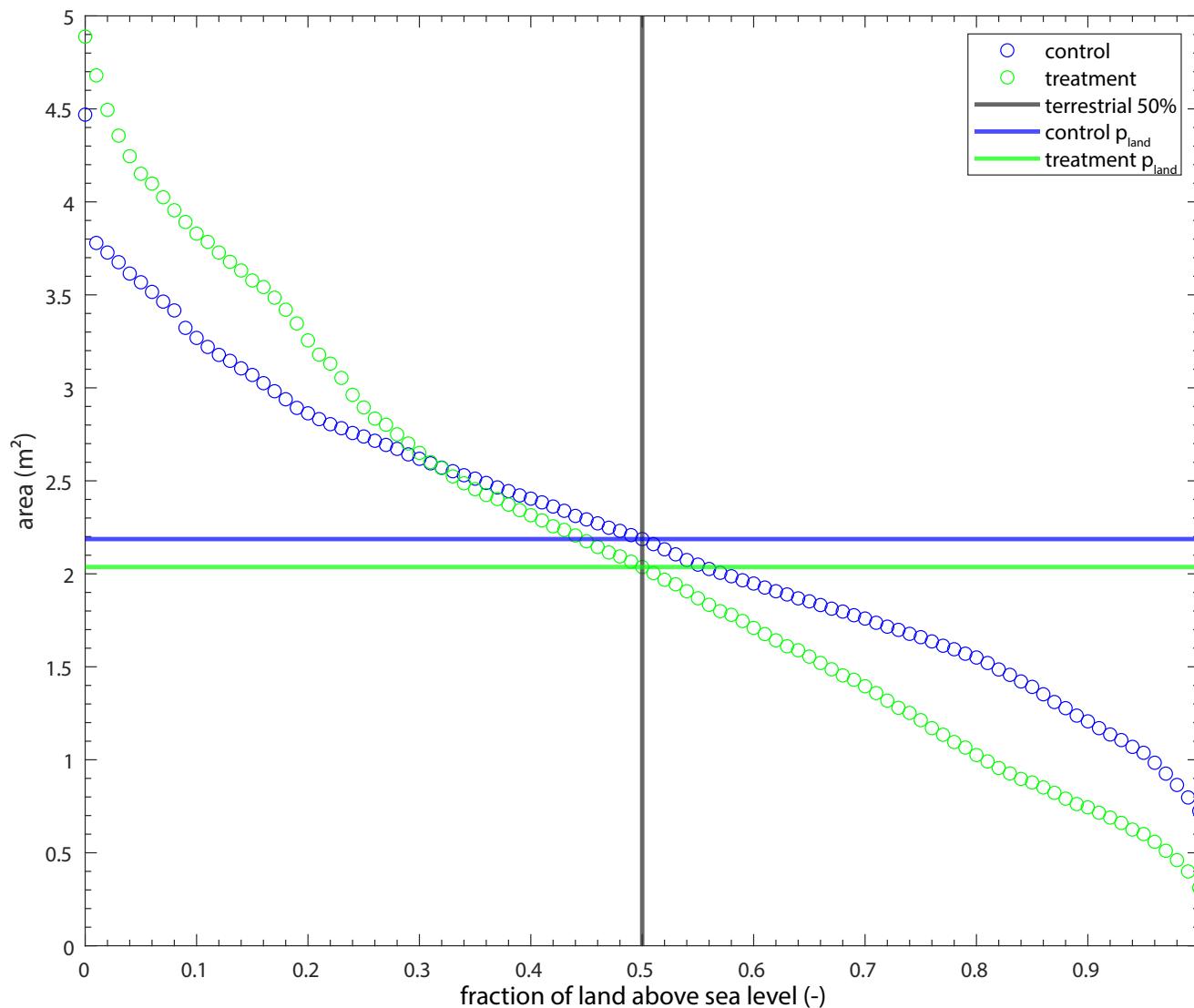
Figure B1. The area of land that is above sea level for various amounts of time for the experiments. The intersection of the black and blue line indicates the area of land (2.2 m^2) that was above sea level for at least 50% of the control experiment (p_{land}). Similarly, the intersection of the black and green line indicates p_{land} (2.0 m^2) for the treatment experiment.

The lateral mobility and modification timescales come from the exponential decay function that describe how quickly the delta top (p_{land}) is visited by channels and how quickly the delta top accumulates sediment (Fig. B2). See Table 1 and Figs. 7a
385 and b for lateral mobility and modification in linear space.

We discuss two different channel movement styles in the results: topographic flow expansions associated with a morphodynamic backwater and lateral movement associated with channel mouth extension and a hydrodynamic backwater. Topographic
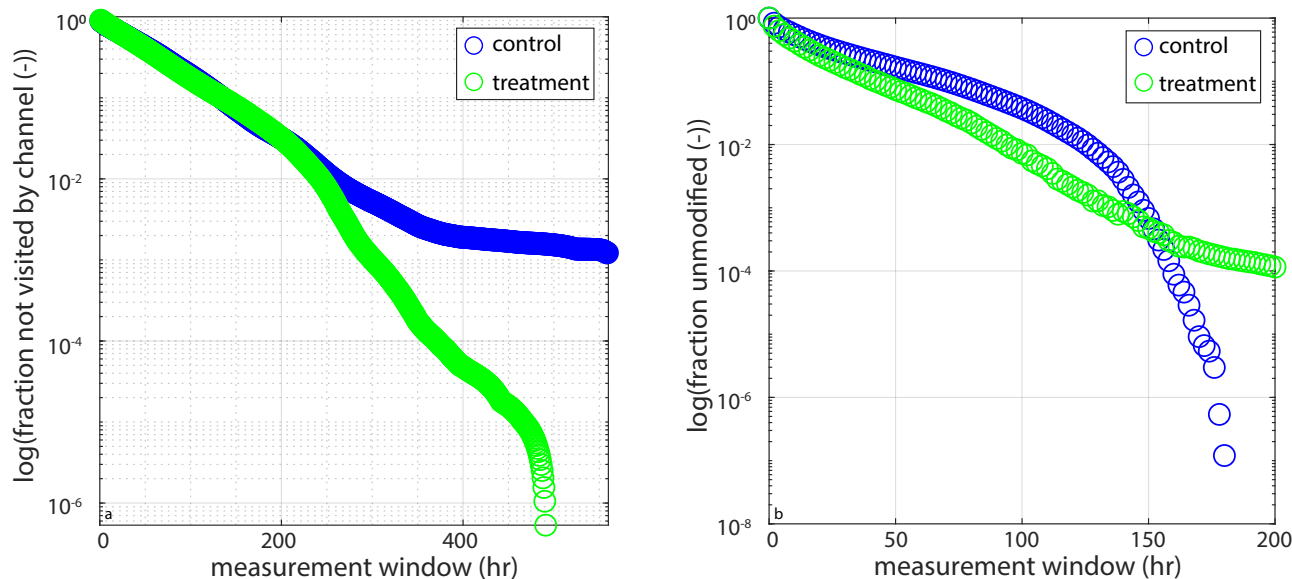
Figure B2. (a) Fraction of the delta that has not been visited by a channel versus measurement window in semilogy space (see Fig. 7a for linear space). (b) Fraction of the delta that has not accumulated at least 1 mm of sediment vesus measurement window in semilogy space (see Fig. 7b for linear space).

flow expansions are characterized by the mouth of the channel becoming unchannelized sheetflow over the entire depositional lobe (Sittoni et al., 2014). The control experiment is mostly characterized by topographic flow expansions, which lead to chan-
390   nel avulsions, likely because the channel beds are super elevated above relative sea level (Fig. B3). We see that the topographic flow expansions, which happen often in the control experiment and sometimes in the treatment experiment, are characterized by the formation of a main channel with some distributary flow. The distributary flow then begins to expand over the entire mouth bar (sheet flow) causing the main channel to recede and the main channel begins to look for a new path at the final point of recession (avulsion location).
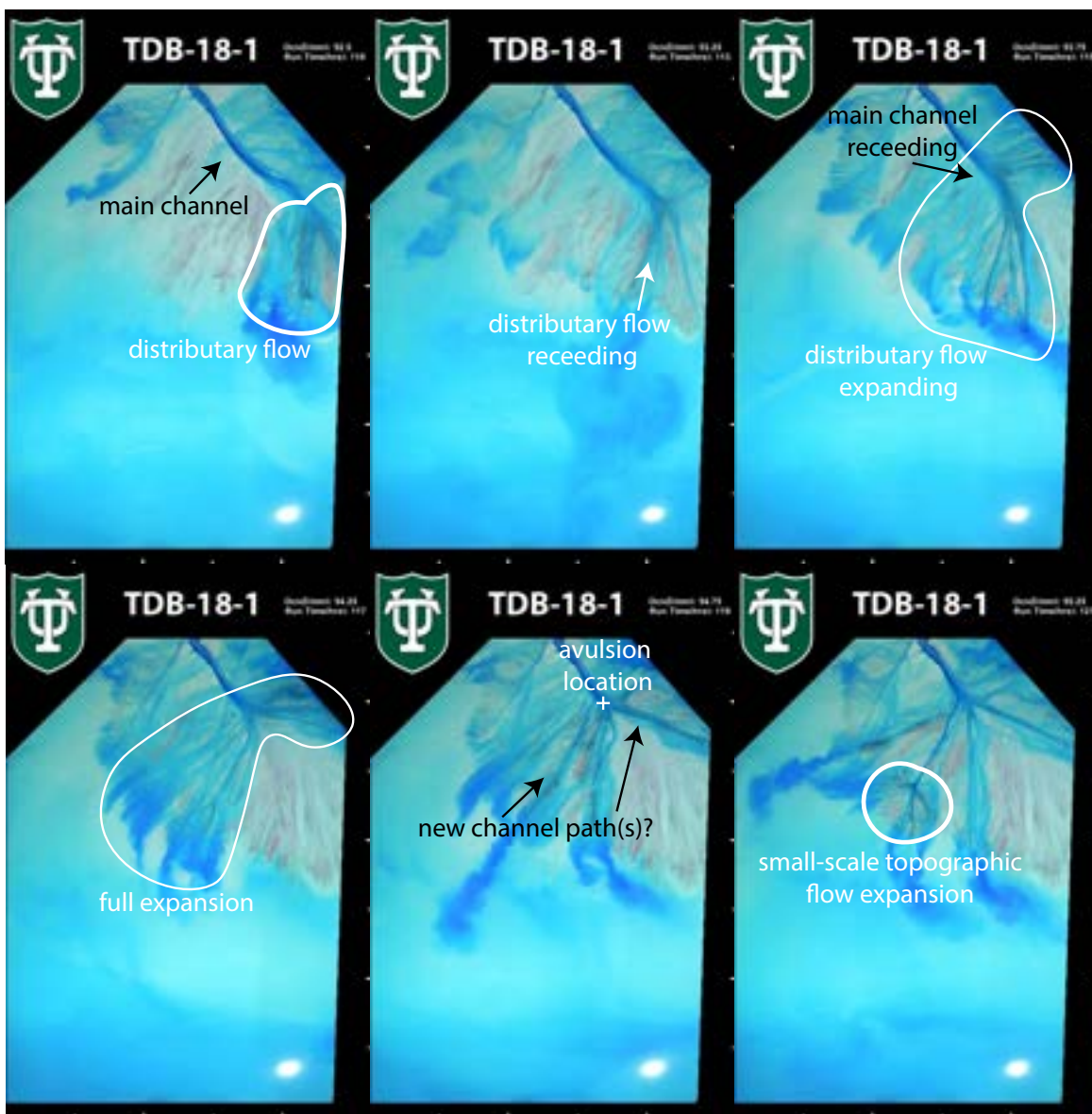
Figure B3. Topographic flow expansion from the control experiment displayed in hours 110, 113, 115, 117, 119, and 121. In this instance, it takes 11 hours for the topographic flow expansion to occur.
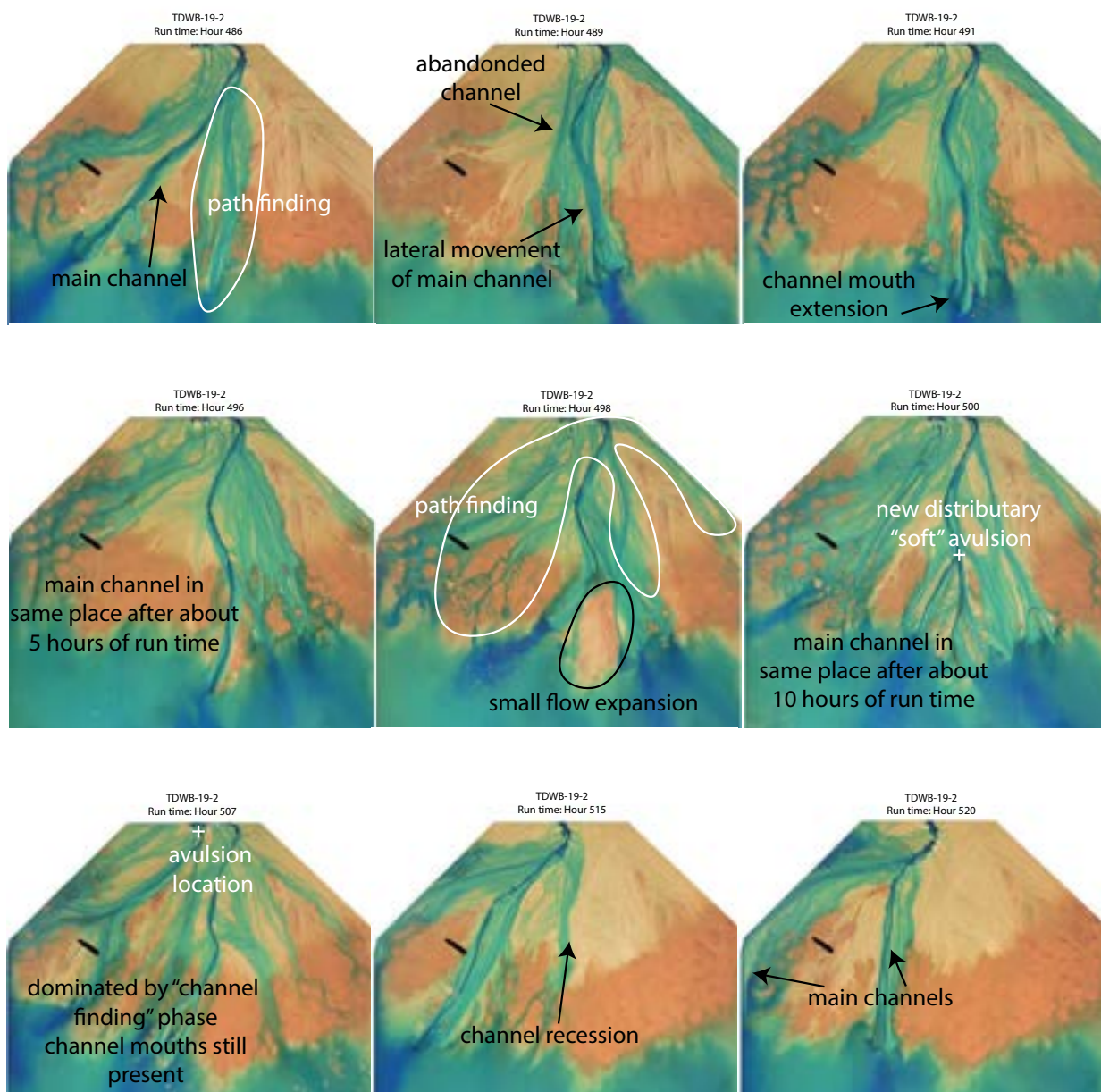
Figure B4. Channel mouth bar formation and lateral switching from the treatment experiment displayed in hours 486, 489, 491, 496, 498, 500, 507, 515, 520. In this example, it takes about 34 hours for lateral movement of main channel.

395   While the treatment experiment does have topographic flow expansions, the channel movement is mostly characterized by the the formation of long lasting channel mouth bars and lateral switching of the channel paths (Fig. B4). We see the formation of a main channel, which occurred due to channel path finding and then lateral movement of the main channel to the new channel location. Upon initiation of the main channel, it begins to extend further into the basin and past the mean shoreline and in this example stays in place for about 10 hours. During this time, smaller channels form on the delta top in the "path finding"

400   phase. A small topographic flow expansion leads to the formation of two distributary channels over the mouth bar (not sheet flow like the control), but ultimately the real avulsion takes place near the entrance channel, where the main channel switches laterally and the old channel is abandoned almost immediately. This process takes longer than the topographic flow expansion, but because of the path finding phase, much of the delta is visited during this time (even though the main channel stays the same).

405   We look at the following channel kinematic metrics: lateral mobility (Li et al., 2017) and fraction of the delta unmodified (Li et al., 2017). We present the findings for the lateral mobility, fraction unmodified, and the number of times a pixel was channelized in the results section of the main text. However, we describe three more channel movement metrics here. The planform overlap metric (Wickert et al., 2013), the number of times a specific location (pixel) on the delta top was channelized, and the longest consecutive channelization for each pixel on the delta top.

410   We use the planform overlap as a check for the lateral mobility of the two systems (treatment and control). Planform overlap is similar to lateral mobiltiy, as it is another commonly used proxy for avulsion timescale in experimental settings (Wickert et al., 2013). Planform overlap is calculated by determining the time it takes for the channel maps to decorrelate from each other. To calculate this, we first calculate the number of changed pixels (channelized to unchannelized or unchannelized to channelized) for each time step (all 1 hour time steps, all 2 hour time steps, etc.). We see that there are less channel pixels

415   changed in the treatment experiment (Fig. B5a). Following methods from Wickert et al. (2013), we scale the number of changed pixels by the number of pixels that would change via random scatter, which gives us ϕ (Phi; Fig. B5b). We again see that there are less changed pixels in the treatment versus the control. We use this change to then determine essentially how long it takes for a channel maps to decorrelate from each other. However, we see that the planform overlap tappers off at roughly the same time in both the control and treatment experiments. The planform overlap exhibits the same exponential decay trend shown by the lateral mobility metrics we used. Thus, we conclude that the lateral mobility of the two systems is similar (Fig.

420   B5c).

       While the lateral mobility timescales do not differ, we do see some subtle differences in channel mobility between the two experiments (Fig. B6). We see that there are more areas on the delta top in the treatment experiment that are rarely visited by a channel, which can be seen by the presence of more dark blue (less visited) areas on the delta top in Fig. B6b (treatment)

425   than Fig. 6a (control). This is supported by the probability distribution of the amount of time each pixel was visited by a channel for the control and treatment experiments (Fig. B6c). The median time a pixel in the control experiment is visited by a channel is 37 hours, but it is slightly shorter in the treatment experiment at 32 hours. Further, we see that more pixels are rarely visited by a channel in the treatment experiment than the control. This suggests that the treatment channels may have some amount of preferential flow (i.e., channels are more likely to reoccupy areas they have already visited) or decreased
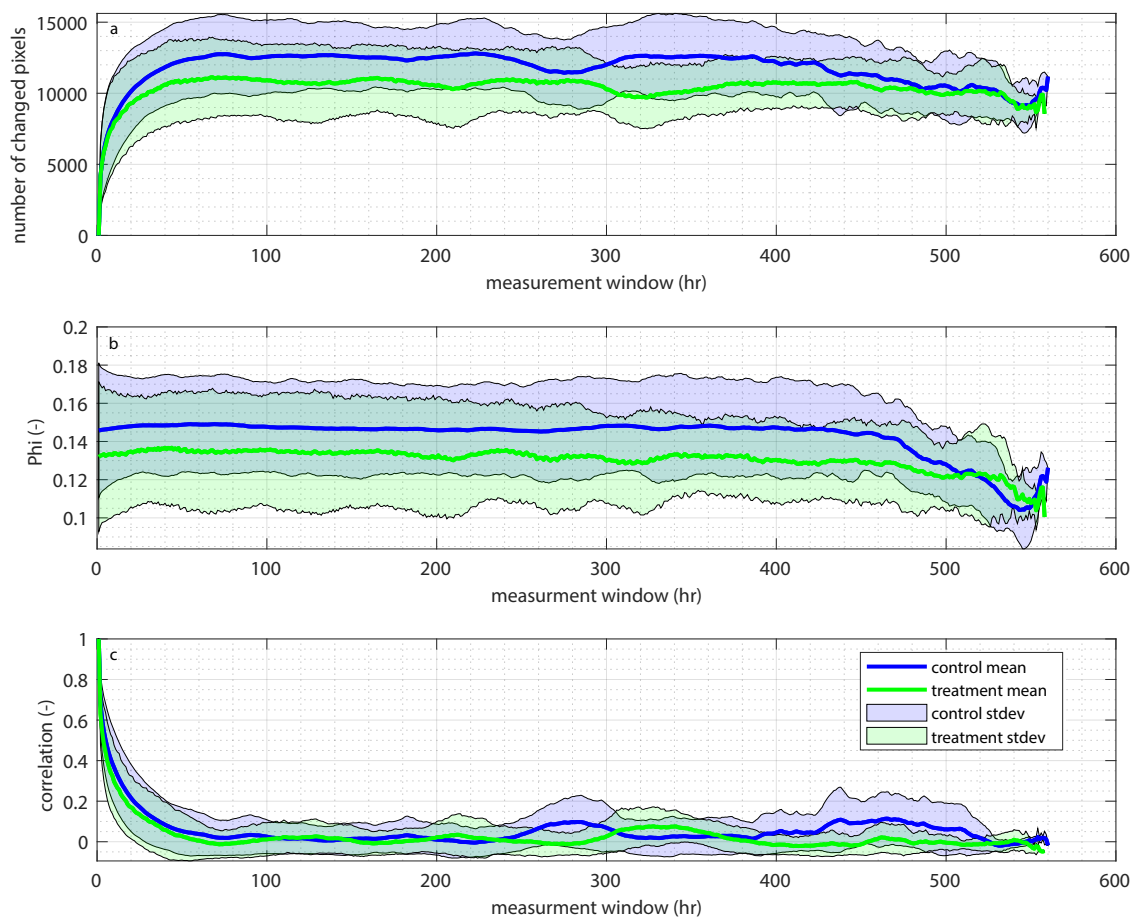
Figure B5. Channel planform change. (a) The mean number of changed channel pixels (y) for various time steps (x) for the control (blue) and treatment (green). The standard deviation is shown as the light blue (control) and light green (treatment) polygons around the mean. (b) The mean number of changed pixels scaled by the number of changed pixels produced via random scatter for the control (blue) and treatment (green). Standard deviation about the mean is shown in light blue for the control and light green for the treatment. (c) The mean time it takes for the channel maps to decorrelate from each other for various time steps for both the control (blue) and treatment (green). The standard deviation about the mean is shown as the light blue (control) and light green (treatment) polygons.

lateral channel mobility combined with efficient sweeping of the channels (supported by the longer channel in-filling timescale in the treatment), even though there is not a decrease in the time it takes the channels to move across the delta top over the delta's life cycle. We also observe a decrease in channel mobility timescale in the treatment experiment due to the presence of a long-lasting channel in the beginning of the experiment (Fig. B8). It is possible that the long-lasting channel in the beginning

off the treatment experiment impacted the average lateral mobility timescale, as the channels had to speed up to fill in the

435   accommodation created by $RSLR_b$.
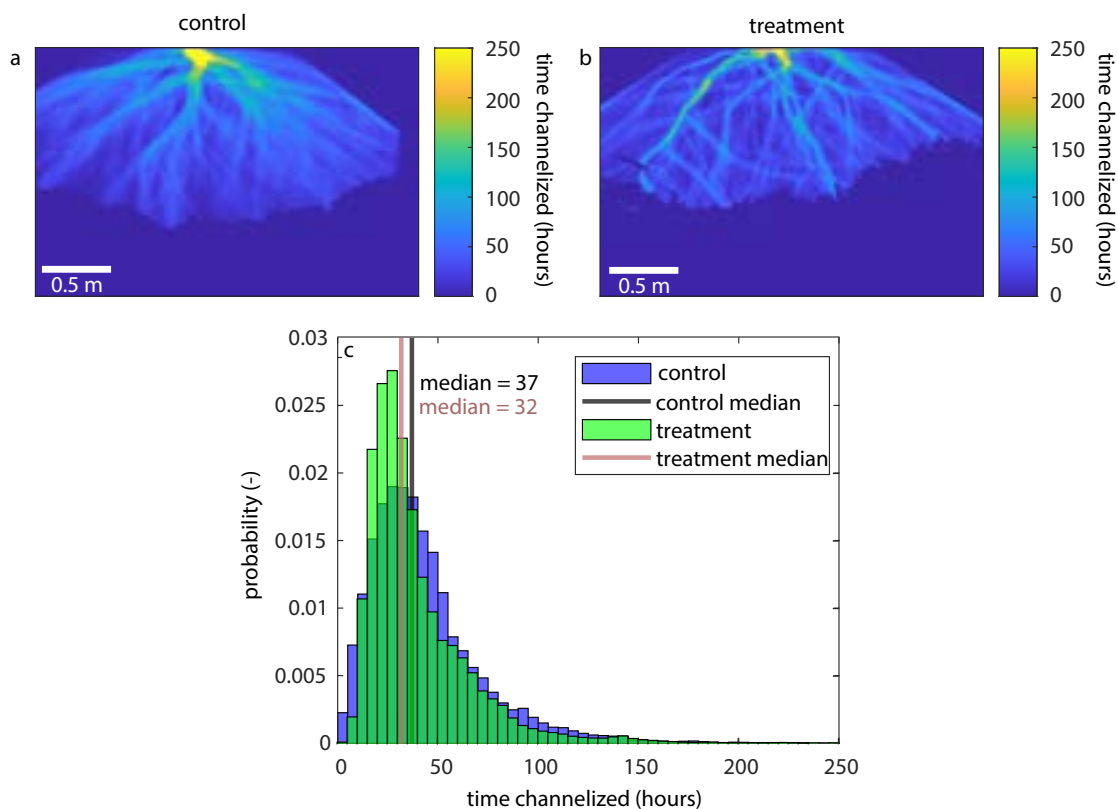
Figure B6. Time each pixel in p_{land} is occupied by a channel. (a, b) The time each pixel in the control (a) and treatment (b) experiments are occupied by a channel. (c) Probability distribution showing the time each pixel is visited by a channel for the control (blue) and treatment (green) experiments.

There is also no clear difference in the amount of consecutive time that channels occupied a specific area (Fig. B7a and b). The main distinction is that channels were able to consecutively occupy an area further from the entrance channel in the treatment experiment than the control experiment. When normalized by the total amount of time a channel occupied that pixel, we again show no significant difference. This normalization shows us that the channel tips tend to be only occupied once, whereas areas near the entrance tend to be occupied many different times (Fig. B7c and d). Finally, we see that a similar pattern

440   emerges in the probability distribution of consecutive channelization (hours; Fig. B7e) as for total channelization (hours) at a pixel (Fig. B6c). There is more area that is not visited by a channel often in the treatment experiment than the control, but

roughly the same amount of area visited by a channel for 50 hours or more consecutively (control = ∼3800 pixels and treatment = ∼3000 pixels; area not shown in Fig. B7e).
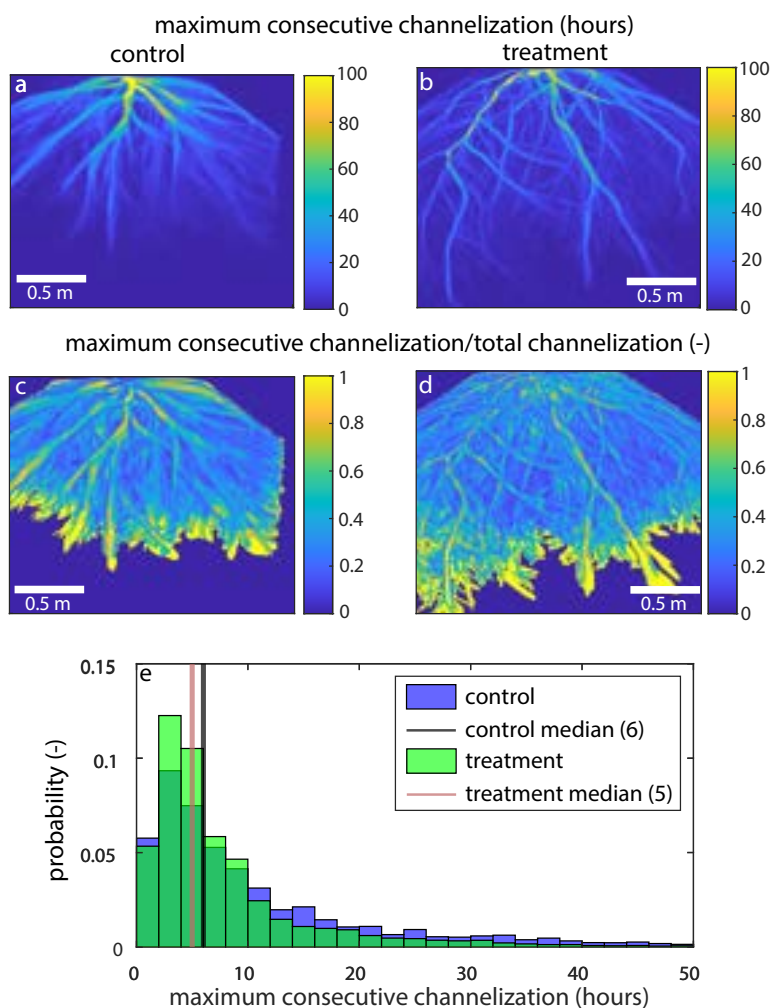
Figure B7. (a, b) The maximum amount of time each pixel in the (a) control and (b) treatment experiments were consecutively channelized (hours) for the entire channelized portion of the delta top. (c, d) The maximum amount of time each pixel in the control experiment was consecutively channelized (hours) divided by the total time each pixel was channelized in the (c) control and (d) treatment for the entire channelized portion of the delta top. (e) The probability distribution for the maximum consecutive time channelized (hours) for the control (blue) and treatment (green).

445   Lastly, we determine the time it takes to approach one e-folding reduction in non-channelized area from each run hour. The average fraction of unchannelized area on the terrestrial delta in the control experiment is ∼0.91 ($1 - \frac{A_c}{p_{land}}$). To get the

e-folding reduction, we divide the unchannelized fraction by e (2.71828), which is ∼0.34. Thus, we calculate the time it takes for channels to visit 66% (1 - 0.34) of the control p_{land}. Similarly, the fraction of unchannelized area in the control experiment is ∼0.89. Reducing by an e-fold, we get 0.33, so we calculate the time it takes for channels to visit 67% of the treatment 450 p_{land}. We do this in order to normalize channel visitation for differences in channel and delta area in the control and treatment experiments. We see that the control experiment oscillates between about 50 and 100 hours. Interestingly, the first ∼200 hours of the treatment experiment have very slow channel mobility (e.g., taking between 80 and 150 hours to visit 67% of the p_{land}), but the last ∼300 hours have very fast lateral channel mobility (e.g., taking between 20 and 60 hours to visit 67% of the p_{land} (Fig. B8). We see that the long-lasting channel(s) in the beginning of the treatment experiment, significantly impacted the 455 channel mobility in the second half of the experiment, potentially speeding up channel motion, so that the delta top could stay in equilibrium.
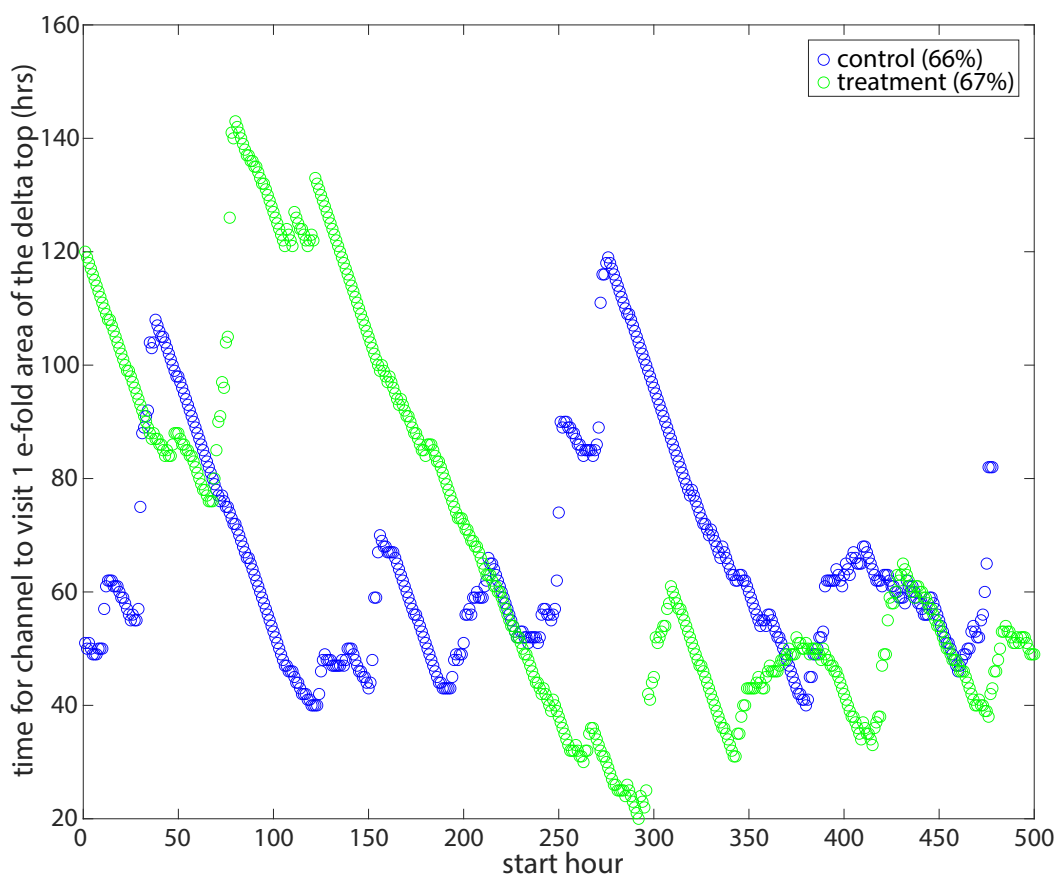
Figure B8. Time to e-folding reduction in non-channelized area of the terrestrial delta in the control (blue) and treatment (green) from each run hour.

Author contributions. KS (Kelly Sanks) performed analysis, created the figures, and wrote the manuscript, with guidance from JBS (John Shaw) and KMS (Kyle Straub); KS, SMZ, JS, JBS, and KMS[2] designed and conducted the treatment experiment and processed various portions of the data; RD (Ripul Dutt) and KMS[2] designed, conducted, and processed data from the control experiment; JBS and KMS[2]

460 acquired funding for the experimental work. All authors reviewed and edited the manuscript.

Competing interests. The authors have no conflicts of interest to disclose.

Acknowledgements. The project was funded by an NSF grant (co PIs Kyle Straub; NSF EAR-1848994 that funded Kyle Straub and Jose Silvestre's time plus much of the experimental costs and John Shaw; NSF EAR-1848993 that funded John Shaw and Sam Zapp's time plus some of the experimental costs). We would like to thank Dr. Eric Barefoot for his monumental help in automating the treatment experiment.

465 # References

Aslan, A., Autin, W. J., and Blum, M. D.: Causes of River Avulsion: Insights from the Late Holocene Avulsion History of the Mississippi River, U.S.A., Journal of Sedimentary Research, 75, 650–664, https://doi.org/10.2110/jsr.2005.053, 2005.

Barefoot, E. A., Nittrouer, J. A., and Straub, K. M.: Non-Monotonic Floodplain Responses to Changes in Flooding Intensity, Journal of Geophysical Research: Earth Surface, 126, e2021JF006 310, https://doi.org/10.1029/2021JF006310, _eprint:
470 https://onlinelibrary.wiley.com/doi/pdf/10.1029/2021JF006310, 2021.

Bhattacharya, J. P.: Delta: Facies Models Revisited, Society for Sedimentary Geology, 84, 237 – 292, 2006.

Caldwell, R. L. and Edmonds, D. A.: The effects of sediment properties on deltaic processes and morphologies: A numerical modeling study, Journal of Geophysical Research: Earth Surface, 119, 961–982, https://doi.org/10.1002/2013JF002965, 2014.

Carlson, B., Piliouras, A., Muto, T., and Kim, W.: Control of Basin Water Depth On Channel Morphology and Autogenic Timescales in
475 Deltaic Systems, Journal of Sedimentary Research, 88, 1026–1039, https://doi.org/10.2110/jsr.2018.52, 2018.

Carlson, B. N., Nittrouer, J. A., Swanson, T. E., Moodie, A. J., Dong, T. Y., Ma, H., Kineke, G. C., Pan, M., and Wang, Y.: Impacts of Engineered Diversions and Natural Avulsions on Delta-Lobe Stability, Geophysical Research Letters, 48, https://doi.org/10.1029/2021GL092438, 2021.

Chadwick, A. J., Lamb, M. P., Moodie, A. J., Parker, G., and Nittrouer, J. A.: Origin of a Preferential Avulsion
480 Node on Lowland River Deltas, Geophysical Research Letters, 46, 4267–4277, https://doi.org/10.1029/2019GL082491, _eprint: https://onlinelibrary.wiley.com/doi/pdf/10.1029/2019GL082491, 2019.

Chadwick, A. J., Lamb, M. P., and Ganti, V.: Accelerated river avulsion frequency on lowland deltas due to sea-level rise, Proceedings of the National Academy of Sciences, 117, 17 584–17 590, https://doi.org/10.1073/pnas.1912351117, publisher: Proceedings of the National Academy of Sciences, 2020.

485 Chadwick, A. J., Steel, E., Williams-Schaetzel, R. A., Passalacqua, P., and Paola, C.: Channel Migration in Experimental River Networks Mapped by Particle Image Velocimetry, Journal of Geophysical Research: Earth Surface, 127, e2021JF006 300, https://doi.org/10.1029/2021JF006300, _eprint: https://onlinelibrary.wiley.com/doi/pdf/10.1029/2021JF006300, 2022.

Chatanantavet, P. and Lamb, M. P.: Sediment transport and topographic evolution of a coupled river and river plume system: An experimental and numerical study, Journal of Geophysical Research: Earth Surface, 119, 1263–1282, https://doi.org/10.1002/2013JF002810, 2014.

490 Chatanantavet, P., Lamb, M. P., and Nittrouer, J. A.: Backwater controls of avulsion location on deltas, Geophysical Research Letters, 39, https://doi.org/10.1029/2011GL050197, 2012.

Coleman, J. M.: Dynamic changes and processes in the Mississippi River delta, Geological Society of America Bulletin, 100, 999–1015, 1988.

Couvillion, B. R., Beck, H., Schoolmaster, D., and Fischer, M.: Land area change in coastal Louisiana (1932 to 2016), USGS Numbered
495 Series 3381, U.S. Geological Survey, Reston, VA, https://doi.org/10.3133/sim3381, code Number: 3381 Code: Land area change in coastal Louisiana (1932 to 2016) Publication Title: Land area change in coastal Louisiana (1932 to 2016) Reporter: Land area change in coastal Louisiana (1932 to 2016) Series: Scientific Investigations Map IP-085820, 2017.

CPRA: Louisiana's Comprehensive Master Plan for a Sustainable Coast, 2017.

Edmonds, D. A. and Slingerland, R. L.: Mechanics of river mouth bar formation: Implications for the morphodynamics of delta distributary
500 networks, Journal of Geophysical Research: Earth Surface, 112, https://doi.org/10.1029/2006JF000574, 2007.

Edmonds, D. A. and Slingerland, R. L.: Significant effect of sediment cohesion on delta morphology, Nature Geoscience, 3, 105–109, https://doi.org/10.1038/ngeo730, 2010.

Edmonds, D. A., Hoyal, D. C. J. D., Sheets, B. A., and Slingerland, R. L.: Predicting delta avulsions: Implications for coastal wetland restoration, Geology, 37, 759–762, https://doi.org/10.1130/G25743A.1, 2009.

505 Elsey-Quirk, T., Graham, S. A., Mendelsohn, I. A., Snedden, G., Day, J. W., Twilley, R. R., Shaffer, G., Sharp, L. A., Pahl, J., and Lane, R. R.: Mississippi river sediment diversions and coastal wetland sustainability: Synthesis of responses to freshwater, sediment, and nutrient inputs, Estuarine, Coastal and Shelf Science, 221, 170–183, https://doi.org/10.1016/j.ecss.2019.03.002, 2019.

Esposito, C. R., Shen, Z., Törnqvist, T. E., Marshak, J., and White, C.: Efficient retention of mud drives land building on the Mississippi Delta plain, Earth Surface Dynamics, 5, 387–397, https://doi.org/10.5194/esurf-5-387-2017, publisher: Copernicus GmbH, 2017.

510 Ganti, V., Chadwick, A. J., Hassenruck-Gudipati, H. J., Fuller, B. M., and Lamb, M. P.: Experimental river delta size set by multiple floods and backwater hydrodynamics, Science Advances, 2, e1501 768, https://doi.org/10.1126/sciadv.1501768, publisher: American Association for the Advancement of Science, 2016a.

Ganti, V., Chadwick, A. J., Hassenruck Gudipati, H. J., and Lamb, M. P.: Avulsion cycles and their stratigraphic signature on an experimental backwater-controlled delta, Journal of Geophysical Research: Earth Surface, 121, 1651–1675, https://doi.org/10.1002/2016JF003915, 515 2016b.

Hajek, E. A. and Wolinsky, M. A.: Simplified process modeling of river avulsion and alluvial architecture: Connecting models and field data, Sedimentary Geology, 257-260, 1–30, https://doi.org/10.1016/j.sedgeo.2011.09.005, 2012.

Holmquist, J. R., Windham-Myers, L., Bliss, N., Crooks, S., Morris, J. T., Megonigal, J. P., Troxler, T., Weller, D., Callaway, J., Drexler, J., Ferner, M. C., Gonneea, M. E., Kroeger, K. D., Schile-Beers, L., Woo, I., Buffington, K., Breithaupt, J., Boyd, B. M., Brown, L. N., Dix, 520 N., Hice, L., Horton, B. P., MacDonald, G. M., Moyer, R. P., Reay, W., Shaw, T., Smith, E., Smoak, J. M., Sommerfield, C., Thorne, K., Velinsky, D., Watson, E., Grimes, K. W., and Woodrey, M.: Accuracy and Precision of Tidal Wetland Soil Carbon Mapping in the Conterminous United States, Scientific Reports, 8, 9478, https://doi.org/10.1038/s41598-018-26948-7, bandiera_abtest: a Cc_license_type: cc_by Cg_type: Nature Research Journals Number: 1 Primary_atype: Research Publisher: Nature Publishing Group Subject_term: Carbon cycle;Climate-change mitigation Subject_term_id: carbon-cycle;climate-change-mitigation, 2018.

525 Holmquist, J. R., Brown, L. N., and MacDonald, G. M.: Localized Scenarios and Latitudinal Patterns of Vertical and Lateral Resilience of Tidal Marshes to Sea-Level Rise in the Contiguous United States, Earth's Future, 9, e2020EF001 804, https://doi.org/10.1029/2020EF001804, _eprint: https://onlinelibrary.wiley.com/doi/pdf/10.1029/2020EF001804, 2021.

Hopkinson, C. S., Morris, J. T., Fagherazzi, S., Wollheim, W. M., and Raymond, P. A.: Lateral Marsh Edge Erosion as a Source of Sediments for Vertical Marsh Accretion, Journal of Geophysical Research: Biogeosciences, 123, 2444–2465, https://doi.org/10.1029/2017JG004358, 530 2018.

Hoyal, D. C. J. D. and Sheets, B. A.: Morphodynamic evolution of experimental cohesive deltas, Journal of Geophysical Research: Earth Surface, 114, https://doi.org/10.1029/2007JF000882, 2009.

Ielpi, A. and Lapôtre, M. G. A.: A tenfold slowdown in river meander migration driven by plant life, Nature Geoscience, 13, 82–86, https://doi.org/10.1038/s41561-019-0491-7, 2020.

535 Jerolmack, D. J. and Swenson, J. B.: Scaling relationships and evolution of distributary networks on wave-influenced deltas, Geophysical Research Letters, 34, https://doi.org/10.1029/2007GL031823, 2007.

Jobe, Z. R., Howes, N. C., Straub, K. M., Cai, D., Deng, H., Laugier, F. J., Pettinga, L. A., and Shumaker, L. E.: Comparing Aggradation, Superelevation, and Avulsion Frequency of Submarine and Fluvial Channels, Frontiers in Earth Science, 8, https://www.frontiersin.org/articles/10.3389/feart.2020.00053, 2020.

540 Kelsall, M., Quirk, T., Wilson, C., and Snedden, G. A.: Sources and chemical stability of soil organic carbon in natural and created coastal marshes of Louisiana, Science of The Total Environment, 867, 161 415, https://doi.org/10.1016/j.scitotenv.2023.161415, 2023.

Khan, N. S., Horton, B. P., McKee, K. L., Jerolmack, D., Falcini, F., Enache, M. D., and Vane, C. H.: Tracking sedimentation from the historic A.D. 2011 Mississippi River flood in the deltaic wetlands of Louisiana, USA, Geology, 41, 391–394, https://doi.org/10.1130/G33805.1, 2013.

545 Kirwan, M. L. and Megonigal, J. P.: Tidal wetland stability in the face of human impacts and sea-level rise, Nature, 504, 53–60, https://doi.org/10.1038/nature12856, 2013.

Kirwan, M. L., Guntenspergen, G. R., D'Alpaos, A., Morris, J. T., Mudd, S. M., and Temmerman, S.: Limits on the adaptability of coastal marshes to rising sea level: ecogeomorphic limits to wetland survival, Geophysical Research Letters, 37, https://doi.org/10.1029/2010GL045489, 2010.

550 Kosters, E. C., Chmura, G. L., and Bailey, A.: Sedimentary and botanical factors influencing peat accumulation in the Mississippi Delta, Journal of the Geological Society, 144, 423–434, https://doi.org/10.1144/gsjgs.144.3.0423, 1987.

Lamb, M. P., Nittrouer, J. A., Mohrig, D., and Shaw, J.: Backwater and river plume controls on scour upstream of river mouths: Implications for fluvio-deltaic morphodynamics, Journal of Geophysical Research: Earth Surface, 117, https://doi.org/10.1029/2011JF002079, 2012.

Lauzon, R. and Murray, A. B.: Comparing the Cohesive Effects of Mud and Vegetation on Delta Evolution, Geophysical Research Letters,
555 45, 10,437–10,445, https://doi.org/10.1029/2018GL079405, 2018.

Leonardi, N., Mei, X., Carnacina, I., and Dai, Z.: Marine sediment sustains the accretion of a mixed fluvial-tidal delta, Marine Geology, 438, 106 520, https://doi.org/10.1016/j.margeo.2021.106520, 2021.

Li, Q., Benson, W. M., Harlan, M., Robichaux, P., Sha, X., Xu, K., and Straub, K. M.: Influence of Sediment Cohesion on Deltaic Morphodynamics and Stratigraphy Over Basin-Filling Time Scales, Journal of Geophysical Research: Earth Surface, 122, 1808–1826,
560 https://doi.org/10.1002/2017JF004216, 2017.

Mohrig, D., Heller, P. L., Paola, C., and Lyons, W. J.: Interpreting avulsion process from ancient alluvial sequences: Guadalope-Matarranya system (northern Spain) and Wasatch Formation (western Colorado), GSA Bulletin, 112, 1787–1803, https://doi.org/10.1130/0016-7606(2000)112<1787:IAPFAA>2.0.CO;2, 2000.

Moodie, A. J. and Nittrouer, J. A.: Optimized river diversion scenarios promote sustainability of urbanized deltas, Proceedings of the National
565 Academy of Sciences, 118, https://doi.org/10.1073/pnas.2101649118, 2021.

Moodie, A. J., Nittrouer, J. A., Ma, H., Carlson, B. N., Chadwick, A. J., Lamb, M. P., and Parker, G.: Modeling Deltaic Lobe-Building Cycles and Channel Avulsions for the Yellow River Delta, China, Journal of Geophysical Research: Earth Surface, 124, 2438–2462, https://doi.org/10.1029/2019JF005220, 2019.

Morris, J. T., Sundareshwar, P. V., Nietch, C. T., Kjerfve, B., and Cahoon, D. R.: Responses of Coastal Wetlands to Rising Sea Level, Ecology,
570 83, 2869–2877, https://doi.org/10.1890/0012-9658, 2002.

Morton, R. A., Bernier, J., Barras, J., and F. Ferina, N.: Historical Subsidence and Wetland Loss in the Mississippi Delta Plain, Transactions of the Gulf Coast Association of Geological Societies, 55, 555–571, 2015.

Mudd, S. M., Howell, S. M., and Morris, J. T.: Impact of dynamic feedbacks between sedimentation, sea-level rise, and biomass production on near-surface marsh stratigraphy and carbon accumulation, Estuarine, Coastal and Shelf Science, 82, 377–389, https://doi.org/10.1016/j.ecss.2009.01.028, 2009.

Nardin, W. and Edmonds, D. A.: Optimum vegetation height and density for inorganic sedimentation in deltaic marshes, Nature Geoscience, 7, 722–726, https://doi.org/10.1038/ngeo2233, 2014.

NASA: How a Delta Forms Where River Meets Lake, https://www.jpl.nasa.gov/images/pia19071-how-a-delta-forms-where-river-meets-lake, 2014.

Nittrouer, J. A., Mohrig, D., and Allison, M.: Punctuated sand transport in the lowermost Mississippi River, Journal of Geophysical Research, 116, https://doi.org/10.1029/2011JF002026, 2011.

Nittrouer, J. A., Best, J. L., Brantley, C., Cash, R. W., Czapiga, M., Kumar, P., and Parker, G.: Mitigating land loss in coastal Louisiana by controlled diversion of Mississippi River sand, Nature Geoscience, 5, 534–537, https://doi.org/10.1038/ngeo1525, 2012.

Nyman, J. A., Walters, R. J., Delaune, R. D., and Patrick, W. H.: Marsh vertical accretion via vegetative growth, Estuarine, Coastal and Shelf Science, 69, 370–380, https://doi.org/10.1016/j.ecss.2006.05.041, 2006.

Paola, C. and Mohrig, D.: Palaeohydraulics revisited: palaeoslope estimation in coarse-grained braided rivers, Basin Research, 8, 243–254, https://doi.org/10.1046/j.1365-2117.1996.00253.x, 1996.

Paola, C., Straub, K., Mohrig, D., and Reinhardt, L.: The "unreasonable effectiveness" of stratigraphic and geomorphic experiments, Earth-Science Reviews, 97, 1–43, https://doi.org/10.1016/j.earscirev.2009.05.003, 2009.

Paola, C., Twilley, R. R., Edmonds, D. A., Kim, W., Mohrig, D., Parker, G., Viparelli, E., and Voller, V. R.: Natural processes in delta restoration: application to the Mississippi Delta, Annual Review of Marine Science, 3, 67–91, https://doi.org/10.1146/annurev-marine-120709-142856, 2011.

Peyronnin, N. S., Caffey, R. H., Cowan, J. H., Justic, D., Kolker, A. S., Laska, S. B., McCorquodale, A., Melancon, E., Nyman, J. A., Twilley, R. R., Visser, J. M., White, J. R., and Wilkins, J. G.: Optimizing Sediment Diversion Operations: Working Group Recommendations for Integrating Complex Ecological and Social Landscape Interactions, Water, 9, 368, https://doi.org/10.3390/w9060368, number: 6 Publisher: Multidisciplinary Digital Publishing Institute, 2017.

Piliouras, A., Kim, W., and Carlson, B.: Balancing Aggradation and Progradation on a Vegetated Delta: The Importance of Fluctuating Discharge in Depositional Systems, Journal of Geophysical Research: Earth Surface, 122, 1882–1900, https://doi.org/10.1002/2017JF004378, 2017.

Prasojo, O. A., Hoey, T. B., Owen, A., and Williams, R. D.: Slope Break and Avulsion Locations Scale Consistently in Global Deltas, Geophysical Research Letters, 49, e2021GL093 656, https://doi.org/10.1029/2021GL093656, _eprint: https://onlinelibrary.wiley.com/doi/pdf/10.1029/2021GL093656, 2022.

Ratliff, K. M., Hutton, E. W. H., and Murray, A. B.: Modeling long-term delta dynamics reveals persistent geometric river avulsion locations, Earth and Planetary Science Letters, 559, 116 786, https://doi.org/10.1016/j.epsl.2021.116786, 2021.

Reed, D. J.: The response of coastal marshes to sea-level rise: Survival or submergence?, Earth Surface Processes and Landforms, 20, 39–48, https://doi.org/10.1002/esp.3290200105, 1995.

Reitz, M. D., Pickering, J. L., Goodbred, S. L., Paola, C., Steckler, M. S., Seeber, L., and Akhter, S. H.: Effects of tectonic deformation and sea level on river path selection: Theory and application to the Ganges-Brahmaputra-Meghna River Delta, Journal of Geophysical Research: Earth Surface, 120, 671–689, https://doi.org/10.1002/2014JF003202, 2015.

610 Sadler, P. M.: Sediment Accumulation Rates and the Completeness of Stratigraphic Sections, The Journal of Geology, 89, 569–584, https://doi.org/10.1086/628623, publisher: The University of Chicago Press, 1981.

Sanks, K. M., Shaw, J. B., and Naithani, K.: Field-Based Estimate of the Sediment Deficit in Coastal Louisiana, Journal of Geophysical Research: Earth Surface, 125, e2019JF005 389, https://doi.org/10.1029/2019JF005389, _eprint: https://onlinelibrary.wiley.com/doi/pdf/10.1029/2019JF005389, 2020.

615 Sanks, K. M., Zapp, S. M., Silvestre, J. R., Shaw, J. B., Dutt, R., and Straub, K. M.: Marsh sedimentation controls delta top morphology, slope, and mass balance, Geophysical Research Letters, https://doi.org/10.1029/2022GL098513, e2022GL098513, 2022.

Shaw, J. B. and McElroy, B.: Backwater number scaling of alluvial bed forms, Journal of Geophysical Research: Earth Surface, 121, 1436–1455, https://doi.org/10.1002/2016JF003861, _eprint: https://onlinelibrary.wiley.com/doi/pdf/10.1002/2016JF003861, 2016.

Shaw, J. B., Mohrig, D., and Wagner, R. W.: Flow patterns and morphology of a prograding river delta, Journal of Geophysical Research:
620 Earth Surface, 121, 372–391, https://doi.org/10.1002/2015JF003570, 2016.

Shaw, J. B., Miller, K., and McElroy, B.: Island Formation Resulting From Radially Symmetric Flow Expansion, Journal of Geophysical Research: Earth Surface, 123, 363–383, https://doi.org/10.1002/2017JF004464, 2018.

Shaw, J. B., Mason, K. G., Ma, H., and McCain III, G. W.: Influences on Discharge Partitioning on a Large River Delta: Case Study of the Mississippi-Atchafalaya Diversion, 1926–1950, Water Resources Research, 57, https://doi.org/10.1029/2020WR028090, 2021.

625 Sittoni, L., Paola, C., and Voller, V.: Geometry, Flow, and Sediment Transport of Alluvial Deposits Induced By Topographically Driven Flow Expansions, Journal of Sedimentary Research, 84, 122–135, https://doi.org/10.2110/jsr.2014.11, 2014.

Slingerland, R. and Smith, N. D.: River Avulsions and Their Deposits, Annual Review of Earth and Planetary Sciences, 32, 257–285, https://doi.org/10.1146/annurev.earth.32.101802.120201, 2004.

Smith, J. E., Bentley, S. J., Snedden, G. A., and White, C.: What Role do Hurricanes Play in Sediment Delivery to Subsiding River Deltas?,
630 Scientific Reports, 5, https://doi.org/10.1038/srep17582, 2015.

Straub, K. M., Paola, C., Mohrig, D., Wolinsky, M. A., and George, T.: Compensational Stacking of Channelized Sedimentary Deposits, Journal of Sedimentary Research, 79, 673–688, https://doi.org/10.2110/jsr.2009.070, 2009.

Straub, K. M., Paola, C., Kim, W., and Sheets, B.: Experimental Investigation of Sediment-Dominated Vs. Tectonics-Dominated Sediment Transport Systems In Subsiding Basins, Journal of Sedimentary Research, 83, 1162–1180, https://doi.org/10.2110/jsr.2013.91, 2013.

635 Tal, M. and Paola, C.: Effects of vegetation on channel morphodynamics: results and insights from laboratory experiments, Earth Surface Processes and Landforms, 35, 1014–1028, https://doi.org/10.1002/esp.1908, 2010.

Törnqvist, T. E. and Bridge, J. S.: Spatial variation of overbank aggradation rate and its influence on avulsion frequency, Sedimentology, 49, 891–905, https://doi.org/10.1046/j.1365-3091.2002.00478.x, _eprint: https://onlinelibrary.wiley.com/doi/pdf/10.1046/j.1365-3091.2002.00478.x, 2002.

640 Valentine, K., Herbert, E. R., Walters, D. C., Chen, Y., Smith, A. J., and Kirwan, M. L.: Climate-driven tradeoffs between landscape connectivity and the maintenance of the coastal carbon sink, Nature Communications, 14, 1137, https://doi.org/10.1038/s41467-023-36803-7, number: 1 Publisher: Nature Publishing Group, 2023.

Wang, Y., Straub, K. M., and Hajek, E. A.: Scale-dependent compensational stacking: An estimate of autogenic time scales in channelized sedimentary deposits, Geology, 39, 811–814, https://doi.org/10.1130/G32068.1, 2011.

645 White, E. D., Meselhe, E., Reed, D., Renfro, A., Snider, N. P., and Wang, Y.: Mitigating the Effects of Sea-Level Rise on Estuaries of the Mississippi Delta Plain Using River Diversions, Water, 11, 2028, https://doi.org/10.3390/w11102028, 2019.

Wickert, A. D., Martin, J. M., Tal, M., Kim, W., Sheets, B., and Paola, C.: River channel lateral mobility: metrics, time scales, and controls, Journal of Geophysical Research: Earth Surface, 118, 396–412, https://doi.org/10.1029/2012JF002386, 2013.

Wilson, C. A. and Goodbred, S. L.: Construction and Maintenance of the Ganges-Brahmaputra-Meghna Delta: Linking Process, Morphology, and Stratigraphy, Annual Review of Marine Science, 7, 67–88, https://doi.org/10.1146/annurev-marine-010213-135032, 2015.

Xu, K., Bentley, S. J., Day, J. W., and Freeman, A. M.: A review of sediment diversion in the Mississippi River Deltaic Plain, Estuarine, Coastal and Shelf Science, 225, 106 241, https://doi.org/10.1016/j.ecss.2019.05.023, 2019.

Zapp, S.: Exploring Sediment Compaction in Experimental Deltas: Towards a Meso-Scale Understanding of Coastal Subsidence Patterns, Graduate Theses and Dissertations, 2020.

650